THICKNESS PREDICTION OF DEPOSITED THERMAL BARRIER COATINGS USING RAY TRACING AND HEAT TRANSFER METHODS

by

Anvesh Dhulipalla

A Thesis

Submitted to the Faculty of Purdue University

In Partial Fulfillment of the Requirements for the degree of

Master of Science in Mechanical Engineering

Department of Mechanical and Energy Engineering at IUPUI

Indianapolis, Indiana

December 2020

THE PURDUE UNIVERSITY GRADUATE SCHOOL
STATEMENT OF COMMITTEE APPROVAL

Dr. Jing Zhang, Chair

Department of Mechanical and Energy Engineering

Dr. Mangilal Agarwal

Department of Mechanical and Energy Engineering

Dr. Shengfeng Yang

Department of Mechanical and Energy Engineering

Approved by:

Dr. Jie Chen

This research is dedicated to my Mother, Father, and Brother, who always supported me.

ACKNOWLEDGMENTS

I want to express my sincere gratitude to my research supervisor, Dr. Jing Zhang, Associate Professor of Mechanical and Energy Engineering at Indiana University - Purdue University Indianapolis, for his guidance and support throughout the project. Furthermore, I would like to extend my gratitude to Dr. Mangilal Agarwal, Director of Integrated Nanosystems Development Institute, Professor of Mechanical and Energy Engineering at Indiana University - Purdue University Indianapolis, Dr. Shengfeng Yang, Assistant Professor of Mechanical and Energy Engineering at Indiana University - Purdue University Indianapolis, for their excellent feedback that helped me reflect on my work and successfully improve it. I would also like to thank Dr. Yafeng Li, School of Mechanical Engineering, Tiangong University, China, for contributing to the heat transfer-based model. Discussion about the ray-tracing model with Dr. Albert Feuerstein, Praxair Surface Technologies (retired), is acknowledged. "Human Resources Program in Energy Technology" of the Korea Institute of Energy Technology Evaluation and Planning (KETEP) granted financial resources from the Ministry of Trade, Industry & Energy, Republic of Korea. (No. 20194030202450) and by the National Research Foundation of Korea (NRF) grant funded by the Korea government (MSIP) (2018R1A5A6075959).

TABLE OF CONTENTS

LIST OF FIGURES

LIST OF TABLES

SYMBOLS AND ABBREVIATIONS

Symbol	Abbreviation
APS	Air Plasma Spraying
α	Alpha angle (radians)
Al	Aluminum
Cr	Chromium
W	Coating deposition rate
d	Coating thickness
do	Coating thickness (original)
ρ	Density
d_s	Thickness at any point
N_w	Number of rays
Tm	Melting point temperature
Ts	Substrate temperature
I_O	Vapor Intensity at α = 0
EB-PVD	Electron Beam Physical Vapor Deposition
fcc	Face-centered cubic
h	Height
ho	Height (original)
kB	Boltzmann constant
M	Mass
m	Molecular weight
n'	Evaporation coefficient
Ni	Nickel
P	Pressure
r	Radial distance
T	Temperature
TBC	Thermal Barrier Coatings
TGO	Thermally grown oxide

θ	Theta angle (radians)
n	Vapor characteristic
vol	Volume
YSZ	Yttria-stabilized zirconia

ABSTRACT

Thermal barrier coatings (TBCs) have been extensively employed as thermal protection in hot sections of gas turbines in aerospace and power generation applications. However, the fabrication of TBCs still needs to improve for better coating quality, such as achieving coating thickness' uniformity. However, several previous studies on the coating thickness prediction and a systematic understanding of the thickness evolution during the deposition process are still missing.

This study aims to develop high-fidelity computational models to predict the coating thickness on complex-shaped components. In this work, two types of models, *i.e.*, ray-tracing based and heat transfer based, are developed. For the ray-tracing model, assuming a line-of-sight coating process and considering the shadow effect, validation studies of coating thickness predictions on different shapes, including plate, disc, cylinder, and three-pin components. For the heat transfer model, a heat source following the Gaussian distribution is applied. It has the analogy of the governing equations of the ray-tracing method, thus generating a temperature distribution similar to the ray intensity distribution in the ray-tracing method, with the advantages of high computational efficiency. Then, using a calibrated conversion process, the ray intensity or the temperature profile are converted to the corresponding coating thickness. After validation studies, both models are applied to simulate the coating thickness in a rotary turbine blade.

The results show that the simulated validation cases are in good agreement with either the experimental, analytical, or modeling results in the literature. The turbine blade case shows the coating thickness distributions based on rotating speed and deposition time. In summary, the models can simulate the coating thickness in rotary complex-shaped parts, which can be used to design and optimize the coating deposition process.

1. INTRODUCTION

Thermal barrier coatings (TBCs) (Bose, 2018; Guo et al., 2007) made of low thermal conductivity ceramics have seen increasing application in gas turbine engines to provide thermal insulation to metallic components from hot gas in the machines used for aircraft propulsion and power generation. The use of TBCs and internal cooling of the underlying superalloy components provides a temperature decrease of up to 300 K in the surface of the superalloy component (Xu et al., 2008). They enable engines to operate at temperatures above the superalloy's melting temperature, improving machines' energy efficiency and performance. On the other hand, TBCs reduce the metal temperature, thus improving components' duration capability (Bose, 2018). Usually, a TBC system has a four-layered structure: the ceramic thermal barrier layer, the metallic bond coat layer, a thermally grown oxide layer between the top and bond coats, and the substrate (Ni et al., 2011). Each layer has its own specific physical and chemical properties, which provide the required functions in TBCs. The thermal barrier layer offers thermal protection to the underlying components. This layer also prevents erosion and corrosion of the underlying parts (Xu et al., 2008). The bond coat protects the superalloy substrate from oxidation and balances the thermal incompatibility between topcoat and substrate. Usually, the TBCs are applied either by plasma spraying or electron beam physical vapor deposition (EB-PVD) (Opsahl, 1987).

A high-energy electron beam heats and vaporizes the target material in the EB-PVD process. The target material is deposited on the substrate's surface in the molecular form under high vacuum conditions (Figure 1) (Movchan, 1996). EB-PVD process produces characteristic microstructures with specific desirable attributes (Figure 2). While Plasma spray leads to the pores between the splats oriented parallel to the substrate surface, revealing lower thermal conductivity (0.8–1.1 $W/m-K$), the columnar grain microstructure created by the EB–PVD process contains channels between the columns and pores within the grains which are oriented perpendicular to the substrate surface, exhibiting a higher thermal conductivity (1.5–1.9 $W/m-K$). Conversely, the columnar allocation of the grains allows an escalation in strain tolerance and, hence, EB–PVD TBCs present greater stability compared to plasma sprayed TBCs (Xu & Wu, 2011).

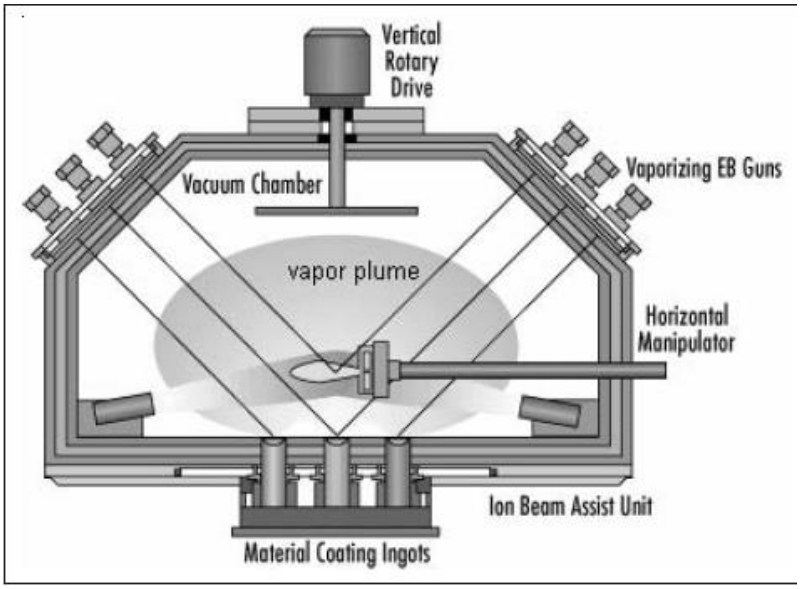

Figure 1. EB-PVD coating chamber. (Fuke et al., 2005)

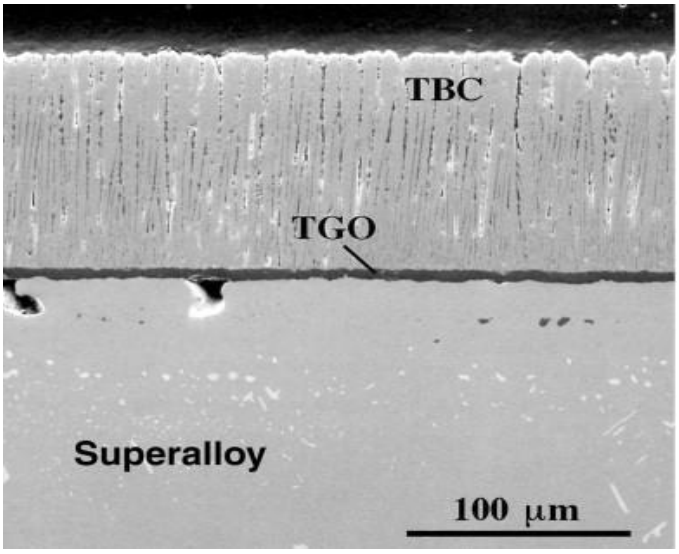

Figure 2. Cross-sectional image of a YSZ TBC deposited by EB-PVD on a superalloy. (Clarke & Phillpot, 2005)

Several constraints affect the quality of coatings, such as substrate temperature (Ts), shape, structure, composition, cleanliness, and the electrical potential difference between the source of evaporation and the substrate. The substrate temperature plays a vital role among these parameters. When the film's thickness surpasses a few hundred nanometers, its crystal structure depends on the substrate temperature (Xu et al., 2008). Suppose the temperature of the substrate is $Ts < 2/3Tm$

(Tm–metal melting point, K), the metal atoms directly condense from vapor into solid phase; when Ts > 2/3 Tm, the metal atoms change from the gas into a liquid phase (droplets). Once the droplets reach a specific size, they can be crystalloid (Yanar et al., 2010).

The following relationship exists between the substrate temperature and the coating microstructure in the classic EB–PVD coating-structural relationship model. When Ts/Tm < 0.3, the coating presents as a dome of the columnar structure due to a self-shadow effect and weak diffusion of the deposited atoms in the substrate's surface (Xu, 2011). In this case, the grain boundary has more pores. When 0.3 < Ts/Tm < 0.5, a dense columnar grain structure forms, and the coating structure forms owing to the condensation controlled by the surface diffusion. In this context, as Ts increases, the grain size of the columnar crystal also increases. And when 0.5 < Ts/Tm < 1, a recrystallization structure forms, which is mainly regulated by volume diffusion (Yanar et al., 2010).

Electron beam physical vapor deposition is a vital evaporation technology to fabricate thermal barrier coatings on superalloy substrates, exceptionally useful for applications on more harsh conditions, such as turbine blades at high pressures (Guo et al., 2007).

1.1 The Motivation for Work

Thermal barrier coatings have been extensively employed as thermal protection in hot sections of gas turbines in aerospace and power generation applications. However, the fabrication of TBCs still needs to improve for better coating quality, such as achieving coating thickness' uniformity. Lack of reliable coating thickness models hinders the extensive employment of the TBCs. Although some studies are focusing on the coating thickness prediction, a systematic understanding is still missing.

1.2 The Objective of the Thesis

The objective of this study is to predict and optimize the coating thickness on complex-shaped components. We achieve this by validating the results with several modeling studies based on the ray-tracing and heat transfer method. In this work, two types of coating thickness prediction models, *i.e.*, ray-tracing based and heat transfer based, are developed. For the ray-tracing model, assuming a line-of-sight coating process and considering the shadow effects, validation studies of coating thickness prediction on different part geometries, including plates, discs, cylinders, and three-pin shaped components. For the heat transfer model, a heat source following Gaussian distribution is applied, which has the analogy of the governing equations of the ray-tracing method, thus generating a temperature distribution similar to the ray intensity distribution in the ray-tracing method, with the advantages of high computational efficiency. After validation studies, both models are applied to simulate the coating thickness in a rotary turbine blade. Finally, using a calibrated conversion process, the ray intensity or the temperature profile are converted to the corresponding coating thickness.

1.3 Structure of the Thesis

The structure of the thesis is as follows. Chapter 2 presents a literature review of the relevant models for simulating coating thickness. Chapter 3 summarizes the governing equations of the ray-tracing and heat transfer models. Chapter 4 presents the validation studies of the model. Chapter 5 shows the model to predict the coating thickness in a turbine blade. Chapter 6 provides the results and discussion of the validation studies and turbine blade model. Chapter 7 gives the conclusions, and Chapter 8 provides the suggested future work.

2. LITERATURE REVIEW

The TBC's primary defect is the uneven distribution of the vaporized target material on the substrate (Chen, 2011). The irregular coating phenomenon is determined using the Ray Tracing technique is used for modeling of TBC. In this approach, the Intensity plot of the number of rays hitting the surface of the turbine blade governs the coating's thickness over the body. In this work first, we try to validate using a plate and then using a disc, cylinder-shaped components, followed by a three-pin component (de Matos Loureiro da Silva Pereira et al., 2017). The validation studies show that the developed model results agree with either the analytical model or experimental measurements. Then the model is applied to a turbine blade to predict its coating distribution.

2.1 Ray-Tracing model for Simulating Coating Thickness in a Three-Pin Cluster with Shadow Effect

It is now well established that the directionality of evaporation molecules in a vacuum at low rates from a small area source leads to a thickness distribution on a flat surface that follows the law stating that the mass per unit area, Eq. 1 deposited on a surface element is equal to (Lang et al., 1983; Rees, 1995)

$$\frac{dM}{dA} = \frac{Me}{\pi h^2} cos^n \theta \cos \alpha$$

Eq. 1

M_e is the total mass evaporated, θ is the angular displacement of the substrate relative to the normal to the source, n is a coefficient that defines the focus of the source, α is the inclination of the substrate the line of vapor flux, measured from the normal of the substrate, and h is the source to substrate distance as shown in Figure 3 (de Matos Loureiro da Silva Pereira et al., 2017).

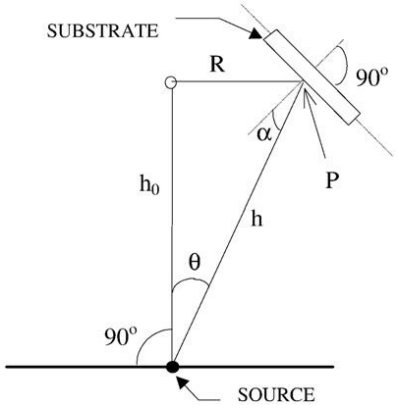

Figure 3. The geometry of evaporation.

However, this simple rule is characteristic only when the vapor emitting surface is a small area compared to the source-to-substrate distance. For the more general case, the thickness deposited is related to the rate of deposition from all sources and the deposition time such that the thickness distribution of a thermally evaporated coating, deposited from an ideal point source evaporator, follows an inverse square law governed by an equation of the form Eq. 2. (Harper, 1978; Maissel & Glang, 1970; Rees, 1995)

$$\frac{d}{d_0} = \frac{h_0^2}{h^2} cos^n\theta \cos\alpha$$

Eq. 2

Where d is the coating thickness at a distance h from the vapor source, d_0 is the thickness directly over the vapor flux at a distance h_0 from the source.

This study replicates the model as per (de Matos Loureiro da Silva Pereira et al., 2017), where two samples from the experimental run are analyzed. The coating thickness is measured around the circular profile, angular displacement varying from 0° to 360°, 0° being point on a cross-section of cylinders facing away from the center of the cluster and 180° closest to the center of the group. Both samples are taken from the same pin.

2.2 Ray-Tracing Model for Simulating Coating Thickness of Disc and Cylinder

In the work of (Fuke et al., 2005), the coating thickness predicted by the computational model agrees well with those predicted by analytical models and experimental results. Here cosine model is used for modeling the shape of the vapor plume generated in EB-PVD. The vapor intensity of the evaporated material can be expressed as Eq. 3:

$$I(\alpha) = I_0 \,.\, cos^n \alpha$$

Eq. 3

$I(\alpha)$ is the vapor intensity in a direction α degree from the normal to vapor emitting surface where I_0 is vapor intensity for α = 0, n = 2, 3, 4…, is an empirical parameter that depends on rate of evaporation.

The cosine model is valid for a small-area evaporator where the diameter of the melt pool, *Dv*, is much smaller than the distance between the melt pool and the substrate, h_v, It should be emphasized that Eq. 3 characterizes the shape of the vapor plume, *i.e.*, it is approximated that the vapor plume has the same shape as the vapor intensity and can be expressed as:

$$r(\alpha) = r_0 . cos^n \alpha$$

Eq. 4

$r(\alpha)$ is the range of vapor plume in a direction α degree from the normal to the vapor emitting surface where r_0 is the range of vapor plume for α = 0 and is assumed as h_v, n = 2, 3, 4,…, is an empirical parameter that depends on the rate of evaporation n.

For a flat plate stationary above the evaporator source for a constant rate of evaporation, the coating film thickness over a given period has been modeled as Eq. 5. (Schiller et al., 1975)

$$\frac{d_s}{d_{so}} = \frac{1}{(1 + \left(\frac{r_s}{h_v}\right)^2)^{\frac{n+3}{2}}}$$

Eq. 5

d_s is the local film thickness,

d_{so} is the film thickness for α = 0

r_s is the distance on the substrate from the point of maximum thickness,

h_v is the height of the substrate over the evaporator source.

Based on Eq. 5, coating film thickness for a cylindrical workpiece is modeled as follows:

$$d_s = d_{so}.\left[\frac{(h_v.cos^2\alpha)}{(h_v + h')^2}\right] \cos(\alpha + \theta)\,.cos^n\,(\alpha)$$

Eq. 6

d_s is the thickness at any point,

d_{so} is the thickness at the point directly above the evaporator and nearest to it,

h_v is the height of the point directly above the evaporator and nearest to it,

h' is the height of any point above h_v,

α is the angle of divergence from the source,

θ is the inclination of the tangent (to the cylinder at a point) to horizontal,

n is the index as suggested in the Schiller model

(*n* = 2 to 6, depending on evaporation rate).

In this approach, we use ray-tracing and heat transfer techniques to validate the experimental data taken from the literature study and then validate them with the computational work. Here we include Plate, Disc, Cylinder, three-pin model.

3. NUMERICAL MODELS OF COATING THICKNESS PREDICTION

3.1 Governing Equations of the Ray-Tracing Method

The ray-tracing method in finite element software numerically solves a set of coupled first-order ordinary differential equations (ODEs) for the components of the quick ray position q and wave vector k. These coupled equations are analogous to the Hamiltonian formulation (Landau & Lifshitz, 1987) in classical mechanics. Eq. 7, Eq. 8, Eq. 9, Eq. 10 are for the ray-tracing module's geometrical optics.

$$\frac{dq}{dt} = \frac{\partial \omega}{\partial k}$$

Eq. 7

$$\frac{dk}{dt} = -\frac{\partial \omega}{\partial q}$$

Eq. 8

$$\frac{\partial q}{\partial t} = \frac{\partial (c|\boldsymbol{k}|/n)}{\partial \boldsymbol{k}} = \frac{c\boldsymbol{k}}{n|\boldsymbol{k}|}$$

Eq. 9

$$\frac{\partial k}{\partial t} = 0$$

Eq. 10

Here the angular frequency ω takes place usually occupied by the Hamiltonian H. When the refractive index is homogeneous, the Hamiltonian formulations above are reduced to the expressions that account for a constant speed and ray direction of light (COMSOL, 2018).

When there is a discontinuity of the refractive index at an interface, the finite element package numerically computes the refracted ray's direction using Snell's law. This formulation makes it possible for the finite element package to calculate exceptional cases with homogeneous refractive indices and more general issues such as thermal lensing in laser engineering (straight rays and

curved rays). Note that this is a time-stepping method available in finite element package, and the results show the beams at different instances of time during propagation (COMSOL, 2018).

3.2 Governing Equations of Heat Transfer-Based Model

In this work, a component is heated up by a heating source to simulate the coating process. The incident heat flux from the heating source has Gaussian distribution on the component's surface. The transient thermal response of the element and its temperature distribution during the heating process is computed. Then the temperature distribution is converted to the coating thickness using a proposed correlation.

The heat transfer equation to describe temperature distribution is defined as (Wessels et al., 2018):

$$\rho C_p \frac{\partial T}{\partial t} = \nabla[k_{th} \nabla T] + Q$$

Eq. 11

where ρ is the material density, C_p the specific heat capacity, T the temperature, t the time, k_{th} the thermal conductivity and Q the heat source in volume due to absorbed heat power.
The heat source term can be written as follows (Wessels et al., 2018):

$$Q = \varepsilon P_{in}(x, t)$$

Eq. 12

where εis the surface emissivity, and P_{in} the incident heat power.
The incident heat power is distributed in time and space with a Gaussian shape. (Wessels et al., 2018)

$$P_{in}(x, t) = P_0 \exp\left\{-\left(\left(\frac{t - t_0}{\tau/2}\right)^2\right)\right\} \exp\left\{-\left(\frac{x}{r}\right)^2\right\}$$

Eq. 13

where P_0 is the peak power, t_0 the time shift, τ the pulse time, r the beam radius at half height.

4. VALIDATION OF THE MODELS

4.1 Ray Tracing Model – Rectangular Plate

4.1.1 Geometry and Finite Element Mesh

The geometry is created by selecting the block feature in the finite element package, and the dimensions are as follows: width of 0.13m, depth of 0.01m, and a height of 0.035m. This geometry is placed in the center at the origin. The plane created is along XY- work plane, as shown in Figure 4.

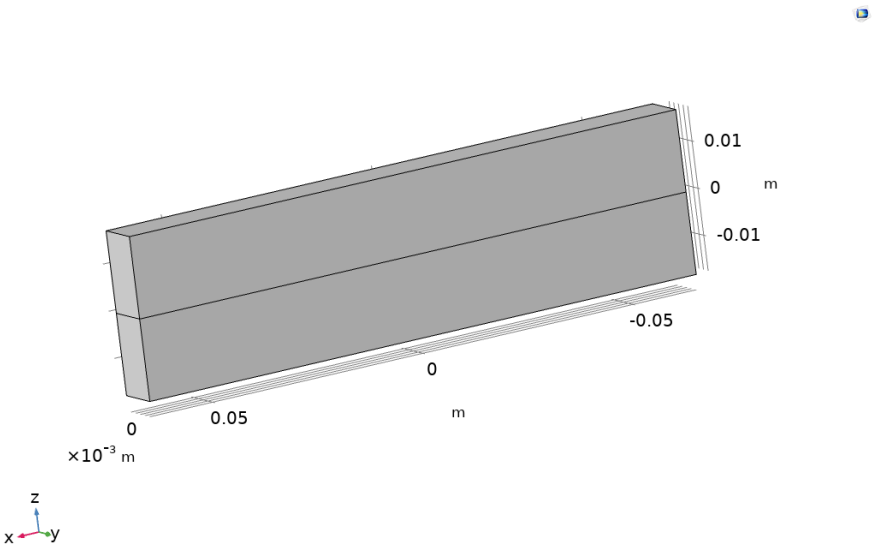

Figure 4. The geometry of the rectangular plate.

A sequence type of physics-controlled is the mesh selection, and the element size is extremely fine, as shown in Figure 5.

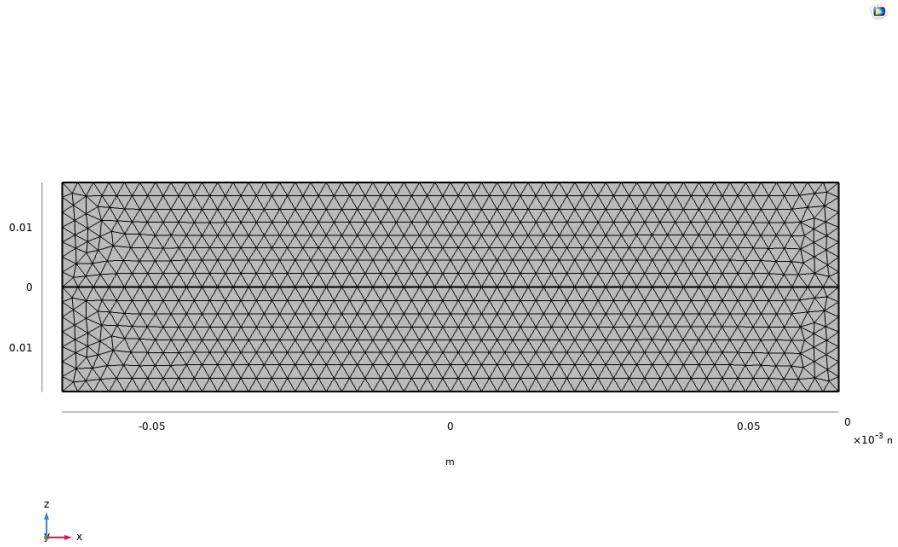

Figure 5. Mesh of a model representing plate in this study.

4.1.2 Material Properties

Here the chosen material is copper, and its properties are shown in Table 1.

Table 1. The material properties for disc

Property	**Value**	**Unit**
Refractive index, real part	0.24	1
Refractive index, imaginary part	0	1
Relative permeability	1	1
Electrical conductivity	$5.998e7[S/m]$	S/m
Coefficient of thermal expansion	$17e-6[1/K]$	$1/K$
Heat capacity at constant pressure	$385[J/(kg*K)]$	$J/(kg\cdot K)$
Relative permittivity	1	1
Density	$8960[kg/m\text{^}3]$	kg/m^3
Thermal conductivity	$400[W/(m*K)]$	$W/(m\cdot K)$
Young's modulus	$110e9[Pa]$	Pa
Poisson’s ratio	0.35	1

Table 1. continued

Reference resistivity	$1.72e-8[ohm*m]$	$\Omega \cdot m$
Resistivity temperature coefficient	$0.0039[1/K]$	$1/K$
Reference temperature	$298[K]$	K

4.1.3 Boundary Conditions

In the settings of geometrical optics module after inserting a wall condition and selecting all the domains of the disc with a freeze condition, a grid of hexapolar type is placed at a location of [0, -0.05,0]m with a cylinder axis direction of [0, -1,0]. The number of radial positions is set to 0. The ray direction vector is set to conical with uniform density, and the number of rays is set to 400000 in the vector space. The cone axis is [0, 1, 0], and the angle is $pi/2$. The vacuum wavelength is 660nm.

4.2 Ray Tracing Model – Disc

4.2.1 Geometry and Finite Element Mesh

The disc has a radius of 22.6 cm and a height of 5 cm. It is positioned at origin and is stationary, as shown in Figure 6. It is stationed at 0.05 m measured along the y-axis from the source, and the ray direction vector is along the (negative) y-axis. The mesh's element size is set to extra fine in the finite element package setup in the geometrical optics module, as shown in Figure 7.

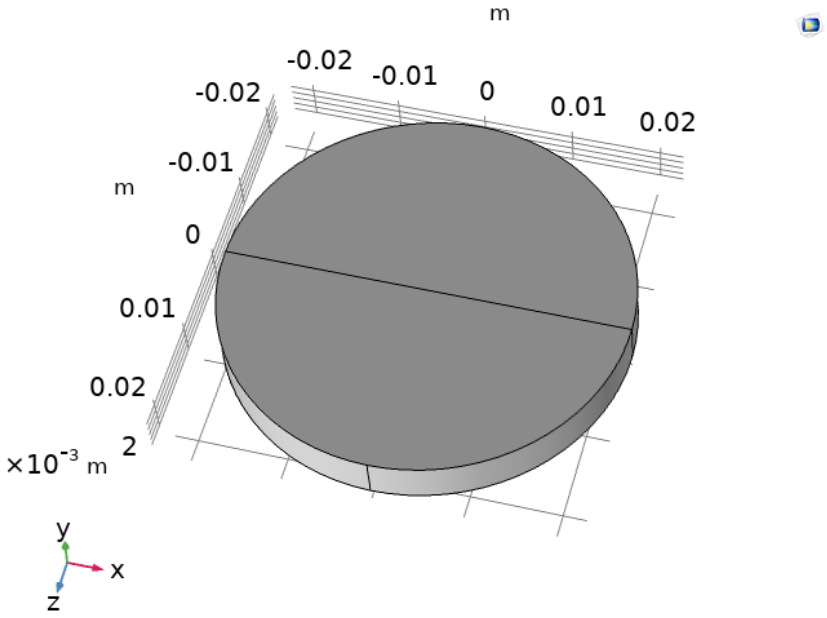

Figure 6. The geometry of disc.

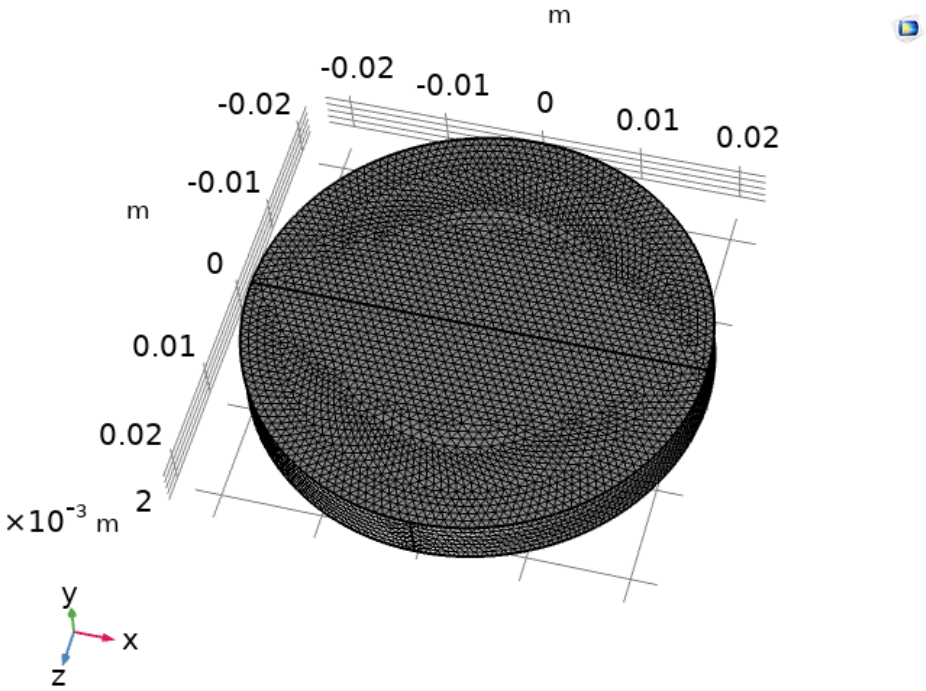

Figure 7. Finite element mesh of disc with a plane in XZ direction passing through the center.

4.2.2 Material Properties

The disc's material properties are similar to that of a rectangular plate, both with the chosen material as copper, and shown in Table 1.

4.2.3 Boundary Conditions

Firstly, In the geometrical optics module, after inserting a wall condition and selecting all the disc domains with a freeze condition, we choose a hexapolar grid type is placed at a location of [0,0.05,0]m with a cylinder axis direction of [0, -1,0] and the number of radial positions is set to 0. The ray direction vector is set to conical with uniform density, and the number of rays is set to 1000000 in the vector space. The cone axis is [0, -1, 0], and the angle is $pi/6$. The vacuum wavelength is 660nm.

4.3 Ray Tracing Model - Cylinder

4.3.1 Geometry and Finite Element Mesh

The cylinder has a radius of 22.6 cm and a height of 0.06 m. It is positioned at origin and is stationary, as shown in Figure 8. In mesh settings, the mesh's element size is selected as a user-defined mesh with free tetrahedral and an element size of 0.00094m with a growth rate of 1.3. The finer mesh is set in the finite element package setup in the geometrical optics module, as shown in Figure 9.

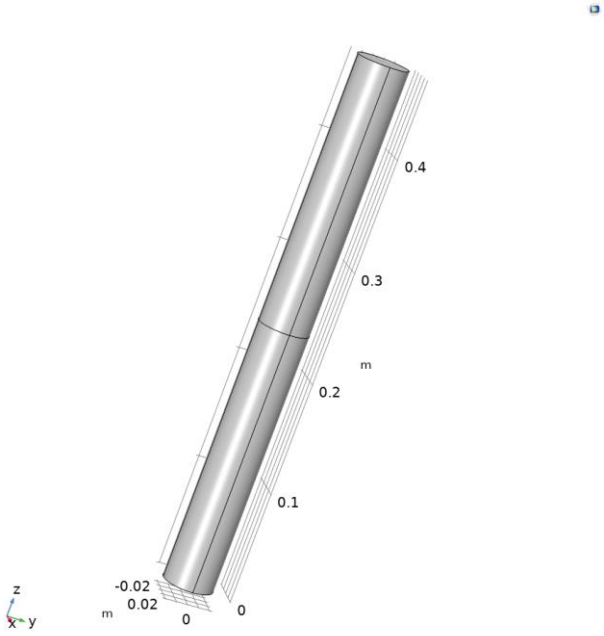

Figure 8. The geometry of the cylinder.

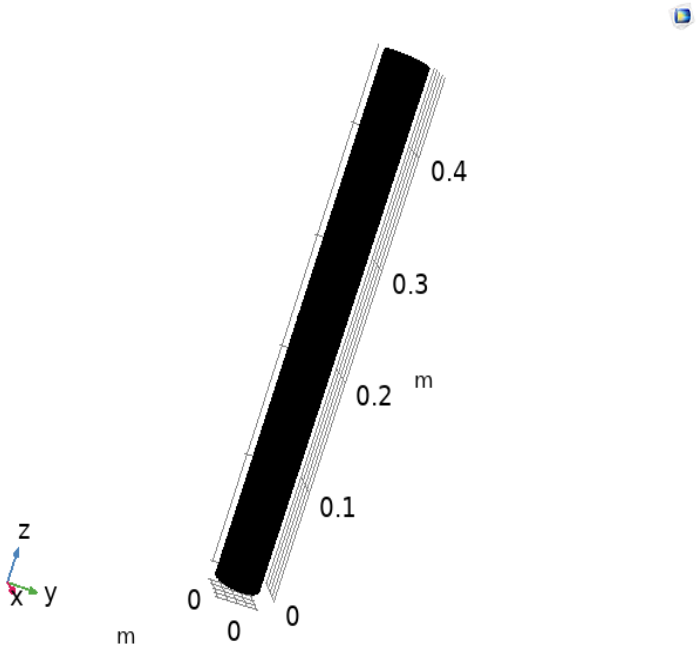

Figure 9.3 Finite element mesh of cylinder with a plane in XY direction through the center.

4.3.2 Material Properties

Here the material is selected as Aluminum, and its properties are shown in Table 2.

Table 2. Material properties of the cylinder

Refractive index, the real part	1.3	1
Refractive index, imaginary part	0	1
Relative permeability	1	1
Heat capacity at constant pressure	$900[J/(kg*K)]$	$J/(kg\cdot K)$
Thermal conductivity	$238[W/(m*K)]$	$W/(m\cdot K)$
Electrical conductivity	$3.774e7[S/m]$	S/m
Relative permittivity	1	1
Coefficient of thermal expansion	$23e-6[1/K]$	$1/K$
Density	$2700[kg/m\text{^}3]$	kg/m^3
Young's modulus	$70e9[Pa]$	Pa
Poisson's ratio	0.33	1
Murnaghan third-order elastic moduli	$-2.5e11[Pa]$	N/m^2
Murnaghan third-order elastic moduli	$-3.3e11[Pa]$	N/m^2
Murnaghan third-order elastic moduli	$-3.5e11[Pa]$	N/m^2
Lamé parameter λ	$5.1e10[Pa]$	N/m^2
Lamé parameter μ	$2.6e10[Pa]$	N/m^2

4.3.3 Boundary Conditions

Firstly, In the geometrical optics module, after inserting a wall condition and selecting all the disc domains with a freeze condition, we choose hexapolar grid type is placed at a location of [0,0.1905,0.4699/2]m with a cylinder axis direction of [0, -1,0] and the number of radial positions is set to 0. The ray direction vector is set to conical with uniform density, and the number of rays is set to 2000000 in the vector space. The cone axis is [0, -1, 0], and the angle is $pi/6$. The vacuum wavelength is 660nm.

4.4 Ray Tracing Model – Three-Pin Component

4.4.1 Geometry and Finite Element Mesh

The coating industry coats multiple blades in a single run to be cost-efficient. This arrangement will limit the deposition on the trailing edge of the other blades. This effect is a result of the shadow of one blade concerning another. This paper discusses how the simulation helps determine the coating thickness with respect to the shadow regions. Three pins are welded to a 6 cm diameter disc to study both the rotational and shadow effects on the thickness distribution. Pins are 0.8 cm in diameter and 10 cm long, positioned in a circle 1.5 cm away from the center of the disc, and at an angular separation of 120° (de Matos Loureiro da Silva Pereira et al., 2017). The disc's center is used as a rotation point, with a rotational speed of 20 rpm. Two planes, 0.1 and 0.3 cm from the base are selected to study the thickness distribution on a cylinder, as shown in Figure 10. The model is scaled to one hundredth so that the simulation performance can be peaked. As shown in Figure 11, The mesh is selected as fine, and the sequence type is physics controlled mesh.

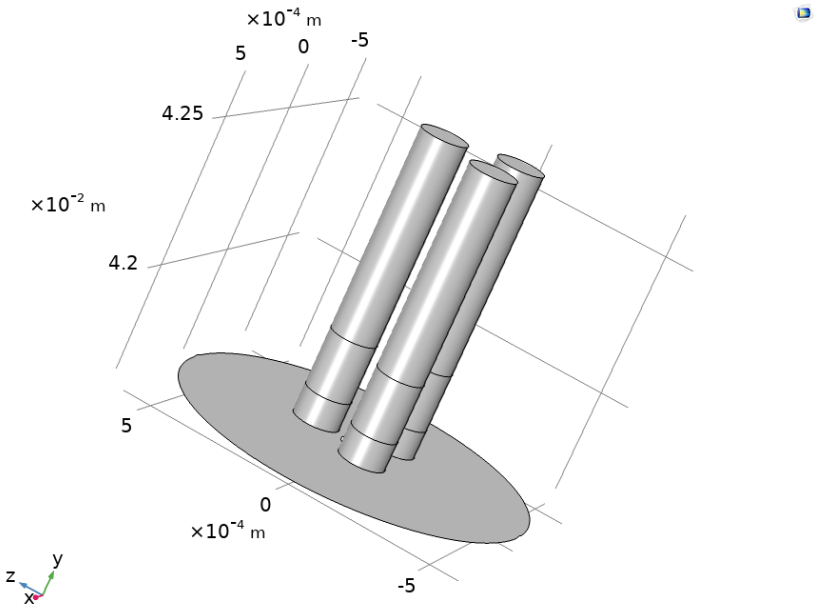

Figure 10. The geometry of the three-pin component.

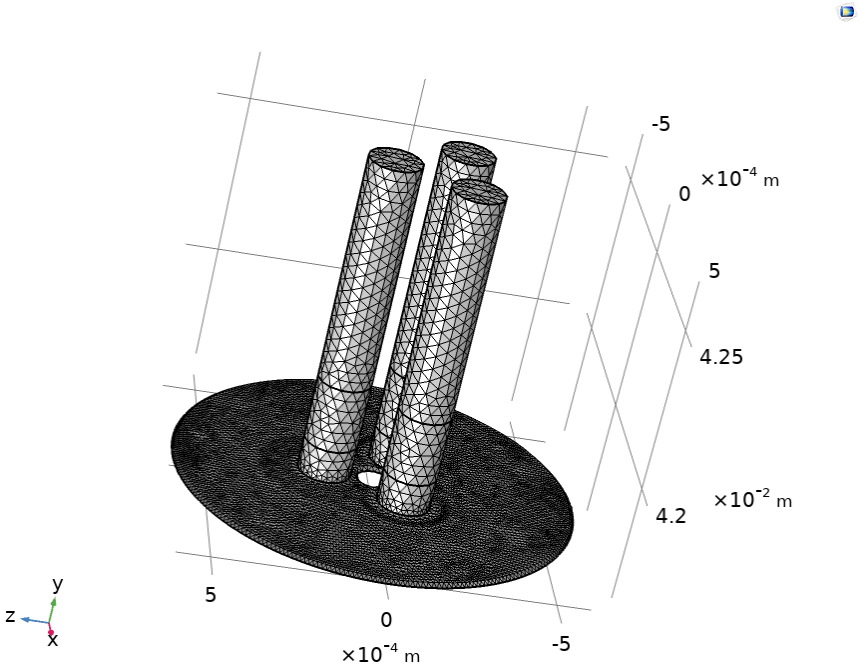

Figure 11. Three-pin mesh with planes at 0.1 and 0.3 cm.

4.4.2 Material Properties

The material properties for the disc are the same as the rectangular plate. Both are selected as Aluminum and are shown in Table 2.

4.4.3 Boundary Conditions

After inserting a wall condition in the geometrical optics module and selecting all the disc domains with a freeze condition, the release times feature is selected, and the distribution function is set to uniform with the setting of a number of values as 10 with a first-time value of 0 and the last value of 9. Grid of hexapolar type is placed at a location of [0,0.0015,0.04225]m with a cylinder axis direction of [-1, 0,0], and the number of radial positions is set to 0. The ray direction vector is set to conical with uniform density, and the number of rays is set to 100000 in the vector space. The cone axis is [-1, 0, 0], and the angle is $pi/6$. The vacuum wavelength is 660nm.

4.5 Heat Transfer Model – Disc and Cylinder

4.5.1 Geometry and Finite Element Mesh

The disc and cylinder models are built in the finite element package. The dimensions are 94.2 mm ×15 mm (D×H) for the disc Figure 12 and 60 mm × 60 mm for the cylinder in Figure 13, so they have the same volume. There are 4,059 3D tetrahedral elements in the disc and 25,980 elements in the cylinder.

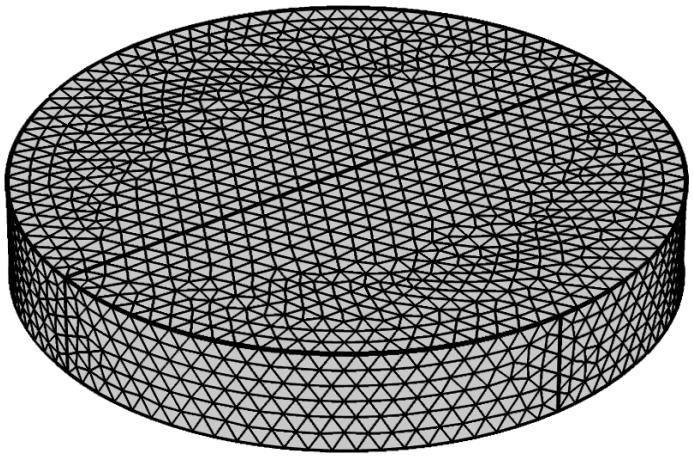

Figure 12. Finite element model of the disc component.

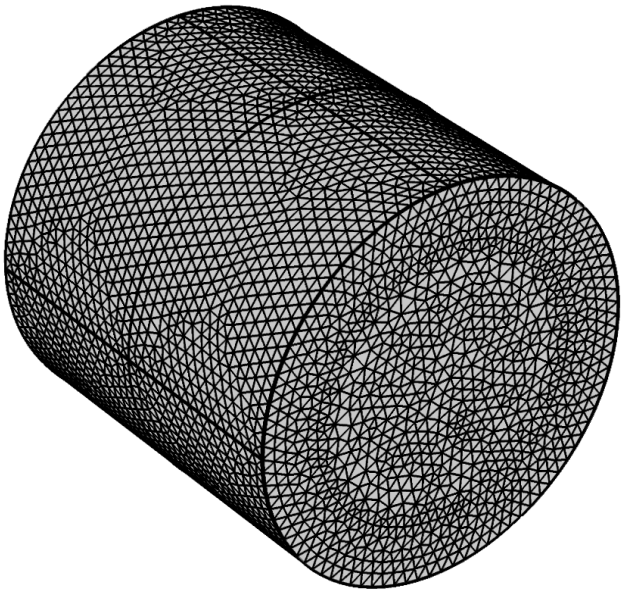

Figure 13. Finite element model of the cylinder component.

Figure 14 shows the three-pin model used (de Matos Loureiro da Silva Pereira et al., 2017). It is a cluster of three pins mounted on a disc and coated in an EB-PVD coater system. since not all dimensions are provided in the reference, the finite element model is reproduced as close as possible as in the reference (de Matos Loureiro da Silva Pereira et al., 2017). In this work, the pins' height is 100 mm, and its diameter is 8 mm. Pins are equally displaced in a triangle shape,

positioned in a circle 15 mm away from the center of the disc, and at an angular separation of 120°. The selection is an extra-fine mesh that has 2,848 3D tetrahedral elements.

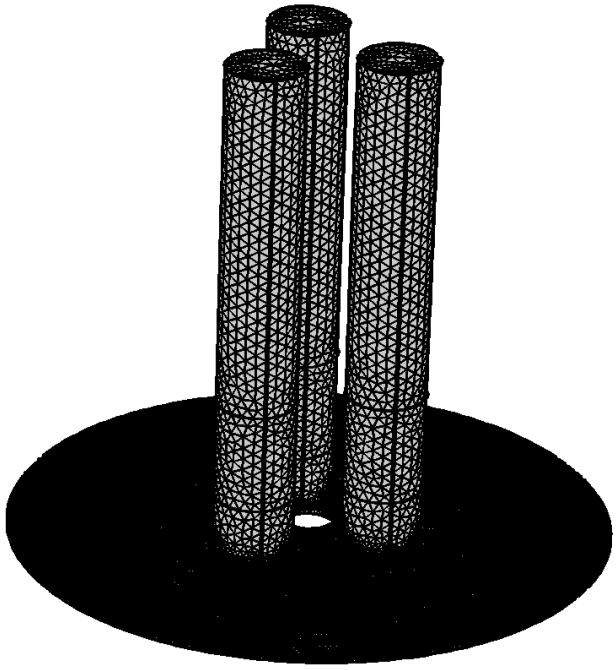

Figure 14. Finite element model of the three-pin component

Figure 15 shows the turbine blade model because of its complexity and industry importance. The turbine blade surface is a complex shape, including both convex and concave surfaces. The height of the model is 3000 μm.

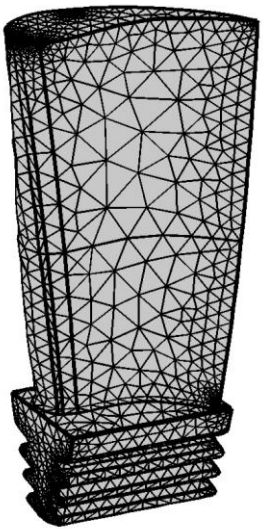

Figure 15. Finite element model of the turbine blade

4.5.2 Boundary Conditions and Material Properties

For the disc and cylinder models, the heating source's diameter is $\pi \times 0.03$ m, covering the whole disc surface and most cylindrical surfaces. The initial temperature is set to 293.15 K. The temperature data are collected along the disk's diameter line and cylinder's half-cycle line.

For the three-pin model, the same as in (de Matos Loureiro da Silva Pereira et al., 2017), the center of the disk is used as the point of rotation of the three-pin structure. The rotation axis is parallel to the disk's normal. A rotational speed of 20 rpm is used. S1 and S2 are the circular profiles on the pin surface. Those are 0.03 m and 0.01 m distant from the disk surface, respectively. For the turbine blade model, the component itself is rotated on its stage at an assumed speed of 20 rpm.

For the material properties, the heat capacity is 385J/(Kg·K), density 8960 kg⁄m^3, and thermal conductivity 400 W/(m·K).

5. PREDICTION OF COATING THICKNESS IN A TURBINE BLADE

5.1 Geometry and Finite Element Mesh

Turbine blade geometry is created using SolidWorks, and then the geometry is scaled to one-tenth to use it to our computational reach of finite element simulation. This model is imported to the finite element package, and then the work planes are created along the XY plane at Z equals 0.05 and a YZ plane. As shown in Figure 16, the mesh is taken as fine, and since few elements are enormous for some small regions, we defined extra fine mesh for a few boundaries, as shown in Figure 17.

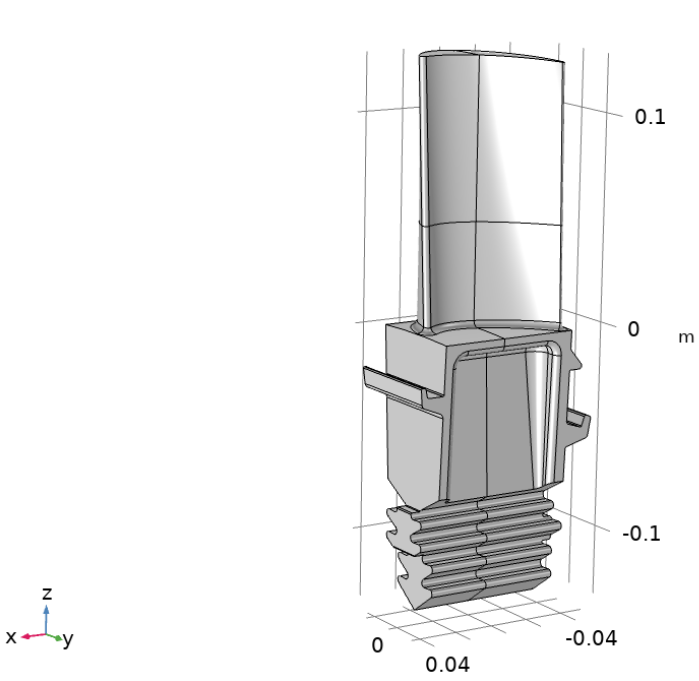

Figure 16. The geometry of the turbine blade.

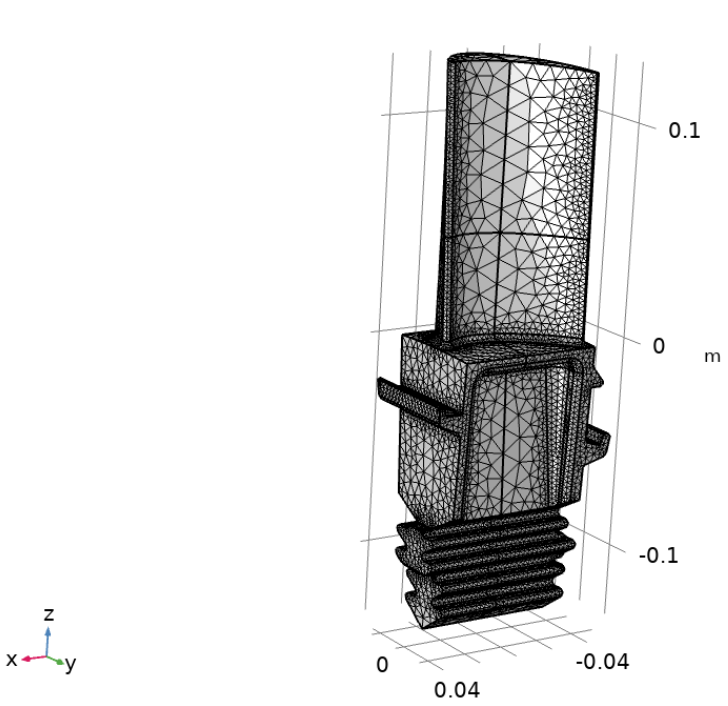

Figure 17. Mesh of the turbine blade.

5.2 Material Properties

The material properties for the disc are the same as the rectangular plate. Both are selected as Aluminum and are shown in Table 2.

5.3 Boundary Conditions

Firstly, in the geometrical optics module, after inserting a wall condition and selecting all the disc domains with a freeze condition, and secondly, we choose the release times to feature is selected. The distribution function is set to uniform with a number of values as 4,10,20 with the first-time value of 0 and the last value of 19. Grid of hexapolar type is placed at a location of [0,0.5,0]m with a cylinder axis direction of [0, 1, 0], and the number of radial positions is set to 0. The ray direction vector is set to conical, and because of the computational constraints with uniform density and number of rays is set to 40000 in the vector space. The cone axis is [0, -1, 0], and the angle is $pi/3$. The vacuum wavelength is 660 nm.

6. RESULTS AND DISCUSSION

6.1 Ray Tracing Model - Rectangular Plate Results

From the data (Fuke et al., 2005; Opsahl, 1987) using the plate and calculating the thickness values for n=12, the model results are conducted on a rectangular plate, Figure 5, and the results are shown below in Figure 18.

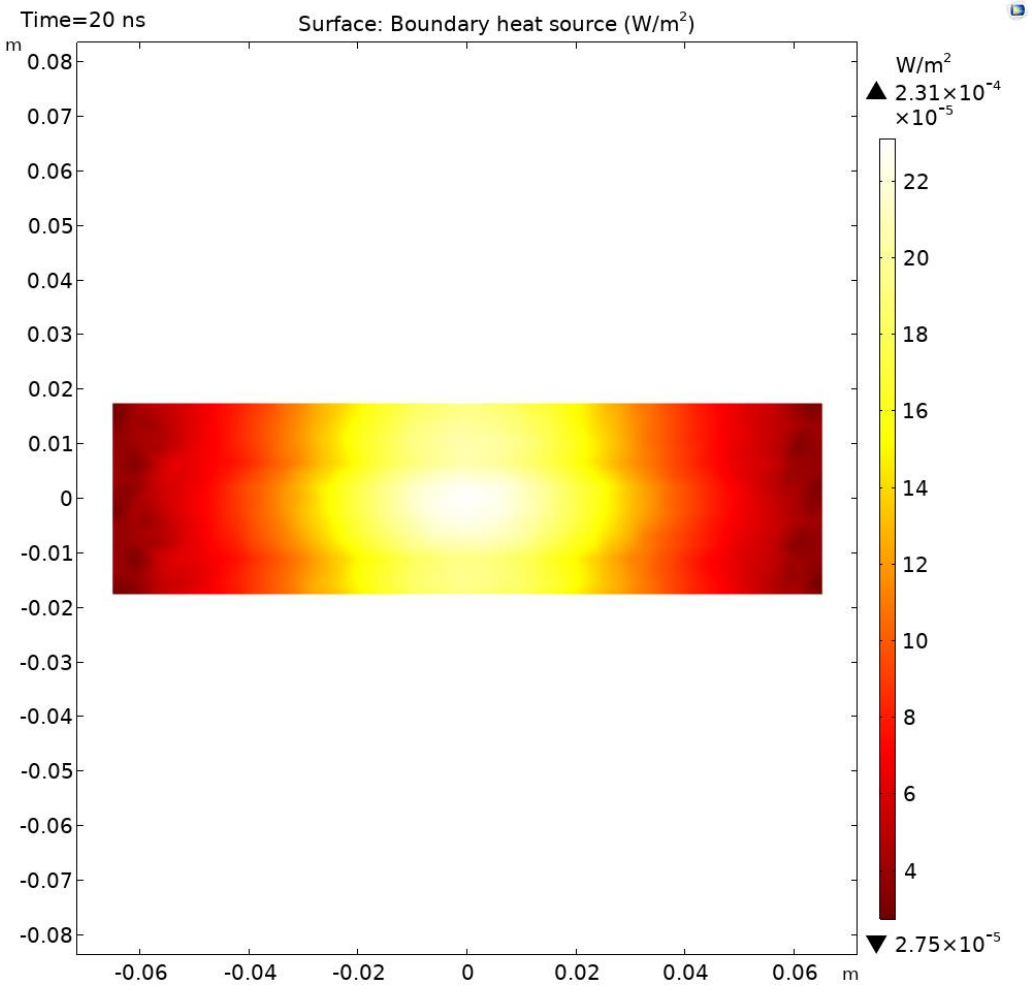

Figure 18. Intensity distribution on a rectangular plate.

After gathering the 3D data from the plate's surface, as shown in Figure 18 and plotting it in Matlab, we get Figure 19. We are scaling the data so that we can compare it with the measured results. We can see that the n value of 12 is the best outcome for the comparison.

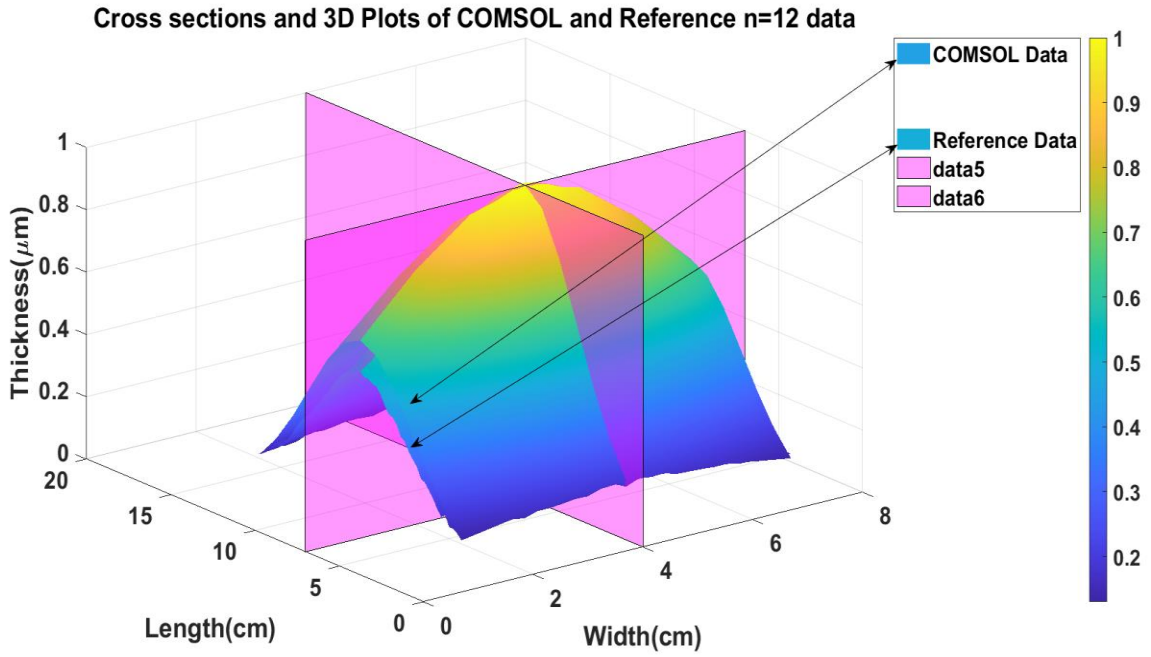

Figure 19. 3D surface plot comparison of finite element model result and reference data.

In Matlab, after drawing the midplanes in length and width directions, Figure 20, Figure 21 shows that for n=12, the finite element model and reference work agree with each other. (Opsahl, 1987)

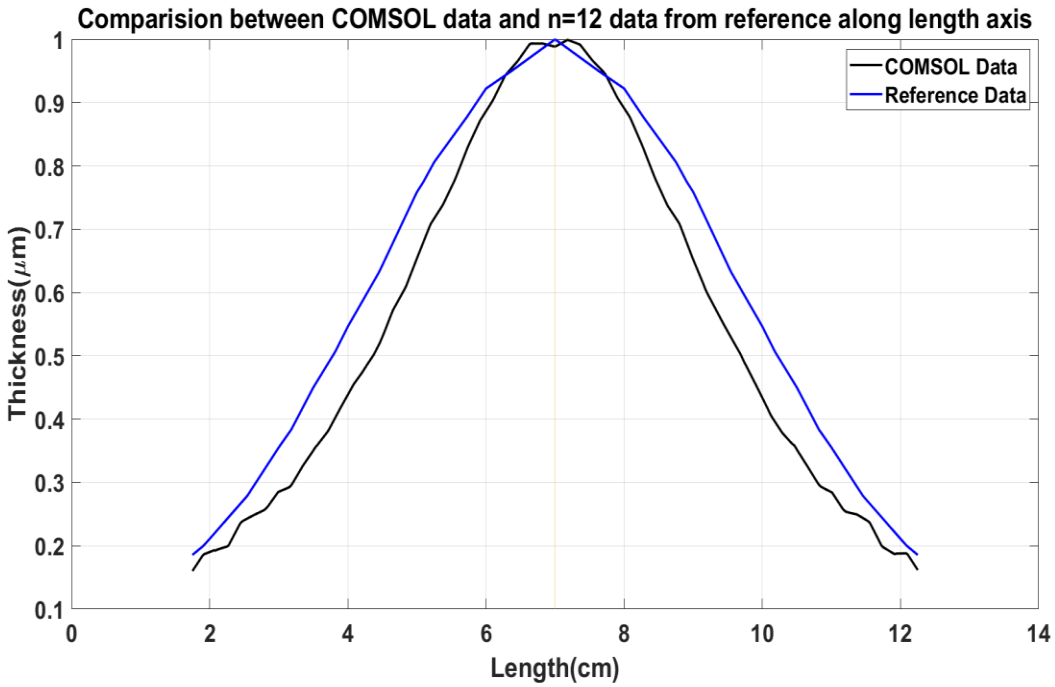

Figure 20. Cross-section graph of comparison for n=12 along the length axis.

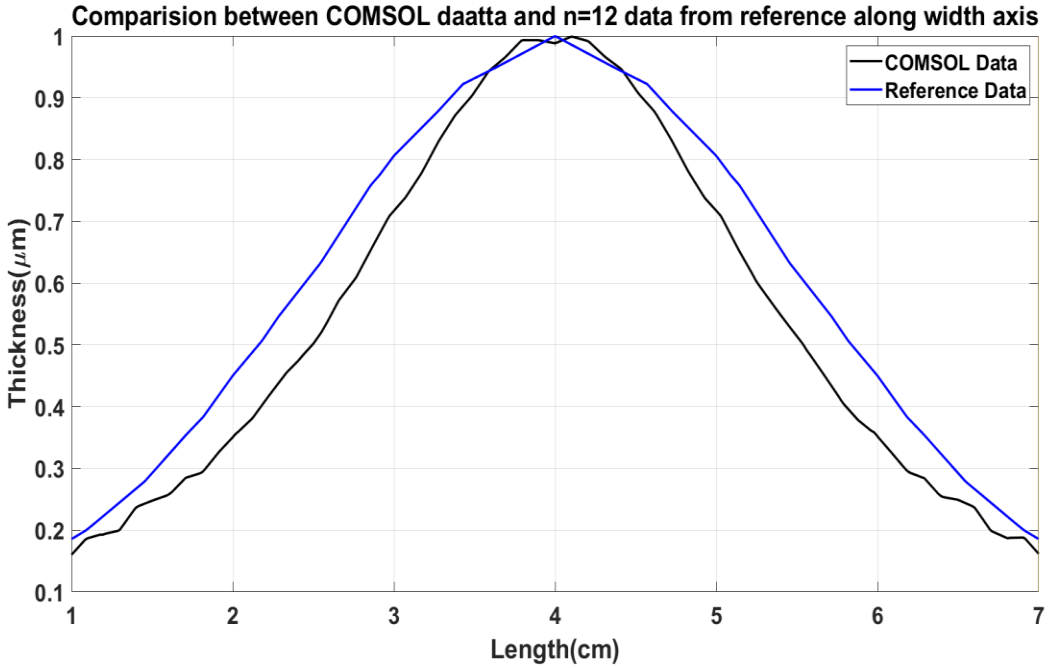

Figure 21. Cross-section graph of comparison for n=12 along the width axis.

6.2 Ray Tracing Model – Disc and Cylinder Results

Figure 22 depicts a 3D plot group of surface intensity on the light illuminating surface. It also shows that intensity has its peak in the center of the disc, and it reduces as we move gradually towards the circumference. In this work, we correlate the power with respect to thickness.

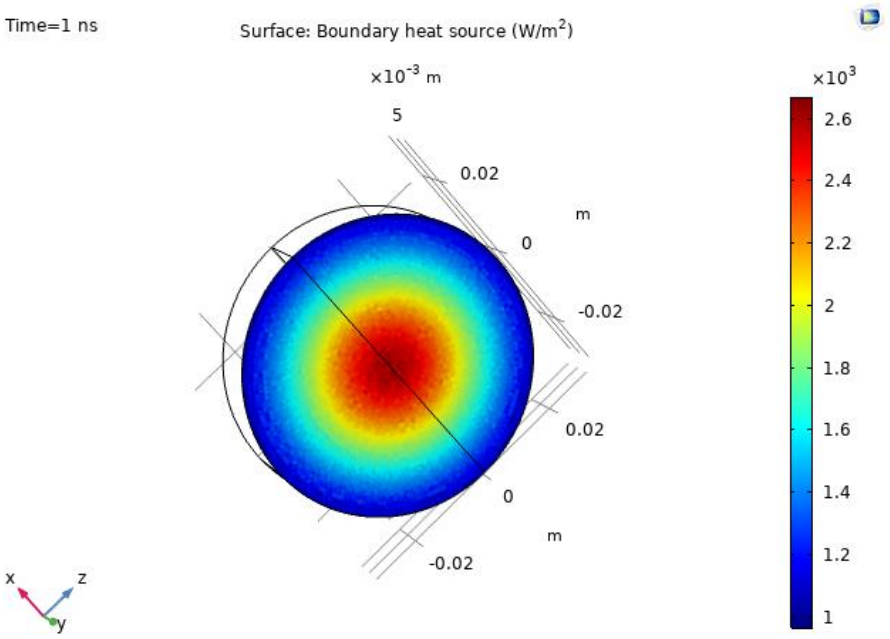

Figure 22. Surface intensity plot on a disc.

Figure 23 shows the intensity vs. arclength profiles of the original finite element model simulation data of disc. It is obtained by scaling the data by x and y as mentioned in Eq. 14, Eq. 15. These are scaled to measure the computational data with the data (Fuke et al., 2005). And the x-axis limits are changed to [-20 20].

$$x = (\ atanb(B(:,1)/0.05));$$

Eq. 14

$$y = B(:,2)/max(B(:,2))$$

Eq. 15

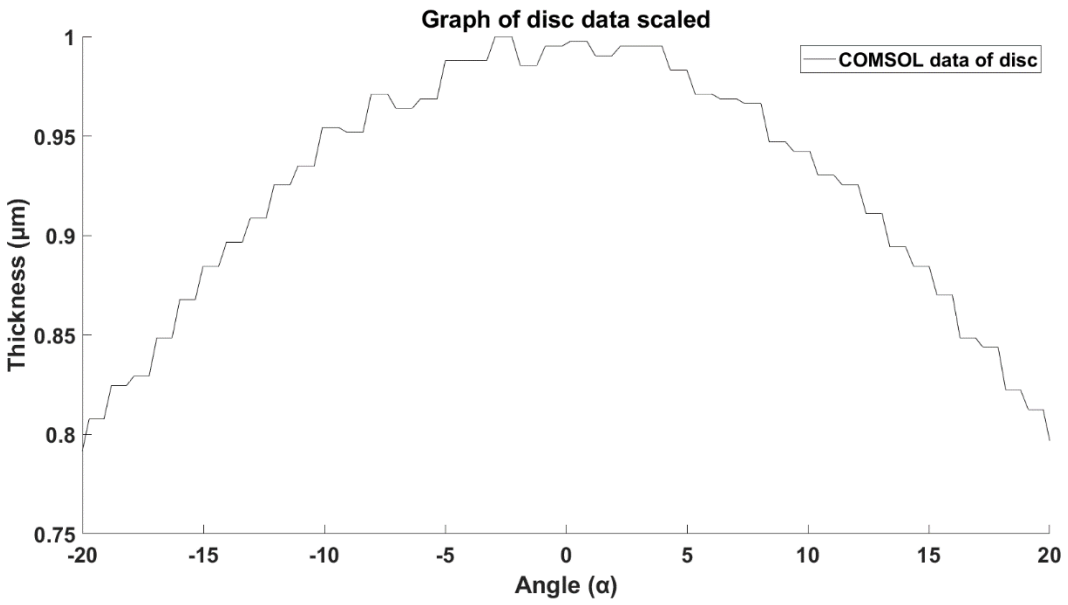

Figure 23. The plot of arc length vs. Intensity of the disc.

Similarly, Figure 24 depicts a 3D plot group of surface intensity on the light illuminating surface. It shows that intensity has its peak in the center of the cylinder. Figure 25 shows the intensity vs. arclength profiles of the cylinder's original finite element model simulation data. It is obtained by scaling the data by X and Y, as shown in Eq. 16, Eq. 17. These are mounted to measure computational data with the data from the (Fuke et al., 2005), and the x-axis limits are changed to [-20 20].

$$x = (\ atanb(A(:,1)/0.05));$$

Eq. 16

$$y = A(:,2)/max(A(:,2))$$

Eq. 17

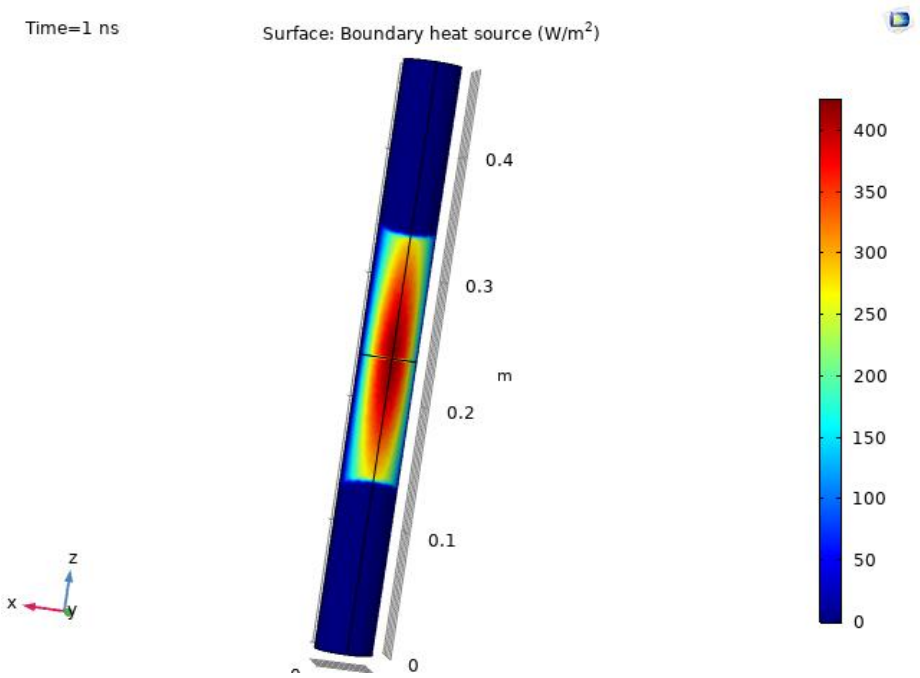

Figure 24. Surface intensity plot on a cylinder.

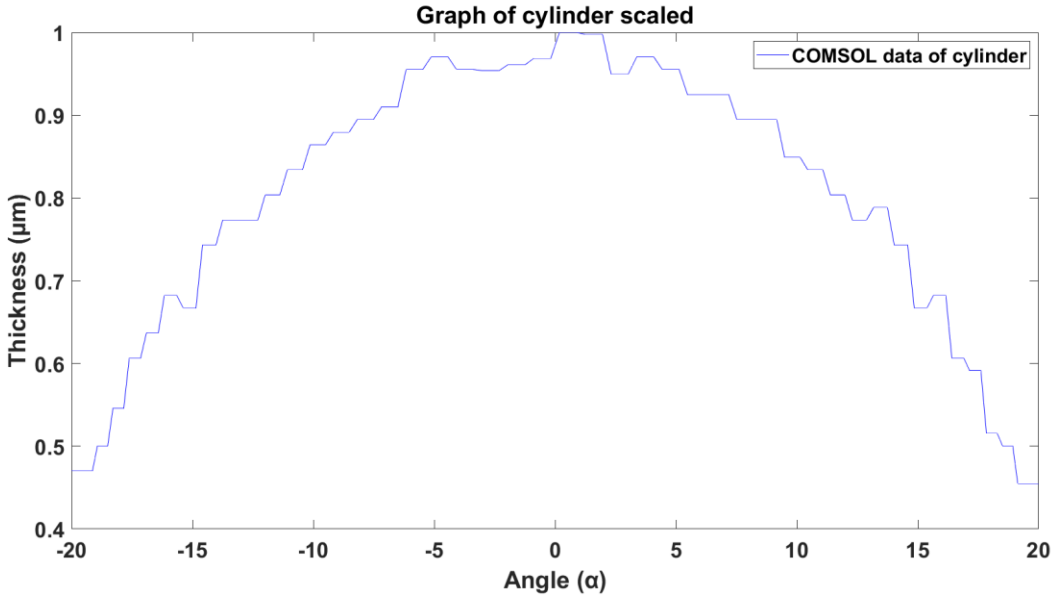

Figure 25. The plot of arc length vs. Intensity of the cylinder.

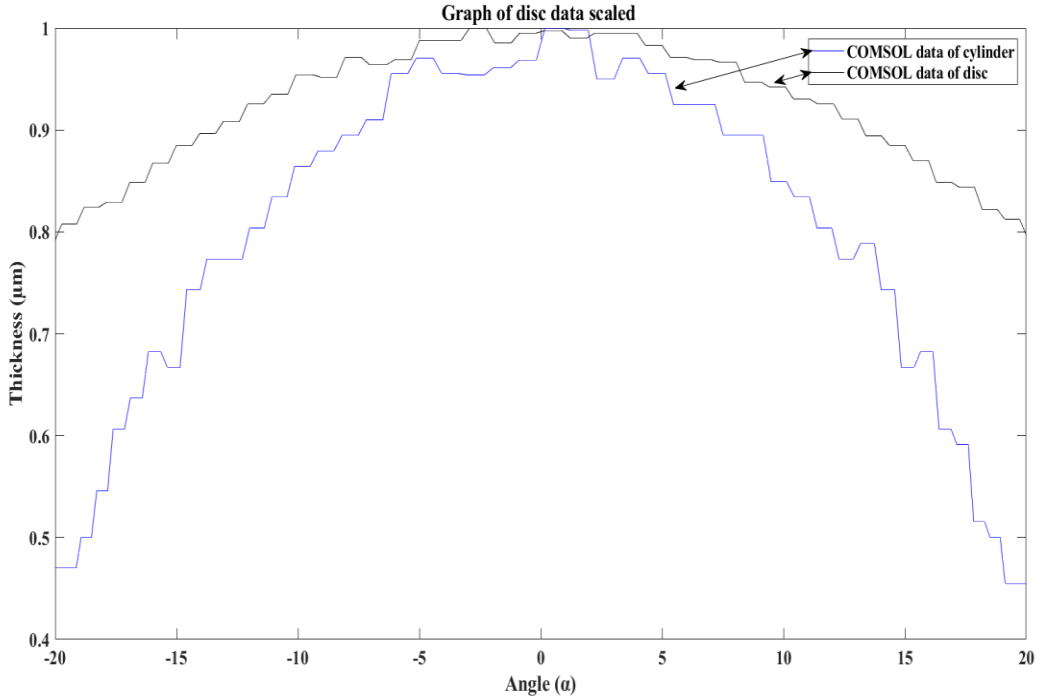

Figure 26. The plot of arc length vs. Intensity of the disc and cylinder after scaling.

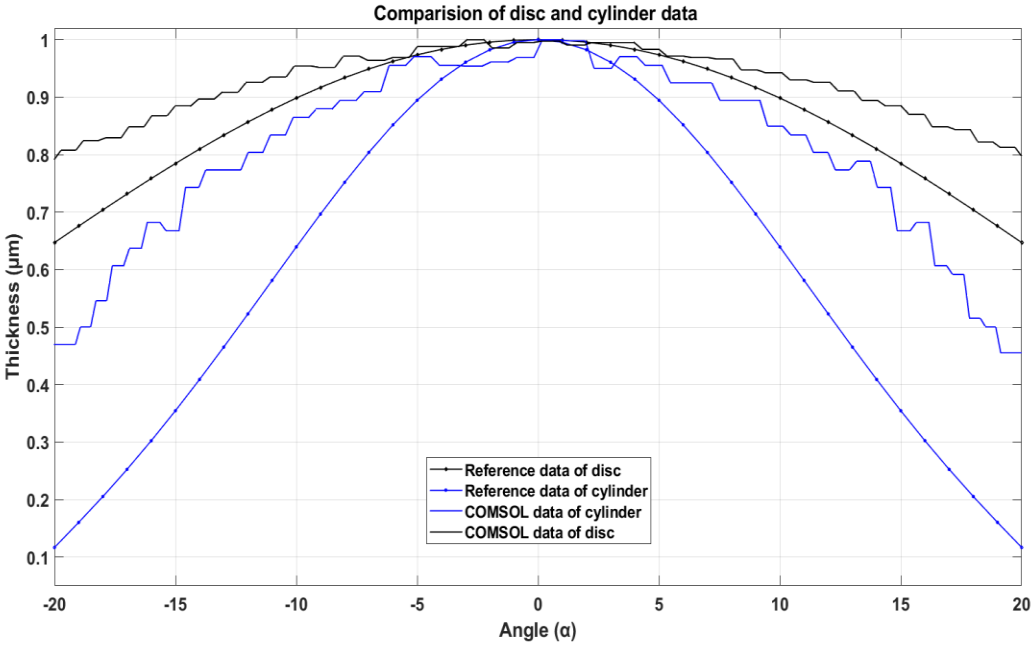

Figure 27. Comparison of finite element model result with reference

Figure 26 depicts that after the Intensity uniformization, the vertex of the disc profile and cylinder profile coincide at a thickness value of 1 μm. The average disc surface intensity is higher than the cylindrical surface intensity because it is a flat surface, whereas the cylinder is a round object. However, the volume, material property, and length of illuminating light collected on the line created by the work plane are identical for the disc and cylinder in the simulation model.

In Figure 27 it shows the coinciding vertex of the disc profile and cylinder profile from the literature (Fuke et al., 2005) analytical model, just because of the same default center maximum film thickness value d_{s0}.

By looking at Figure 27, either disc profile or cylinder profile has the characters of identical shape, tend, and distribution, though they have different physical units and values. That is why they can be related, and the coating thickness can be solved by intensity input.

6.3 Ray Tracing Model – Three-Pin Model Results

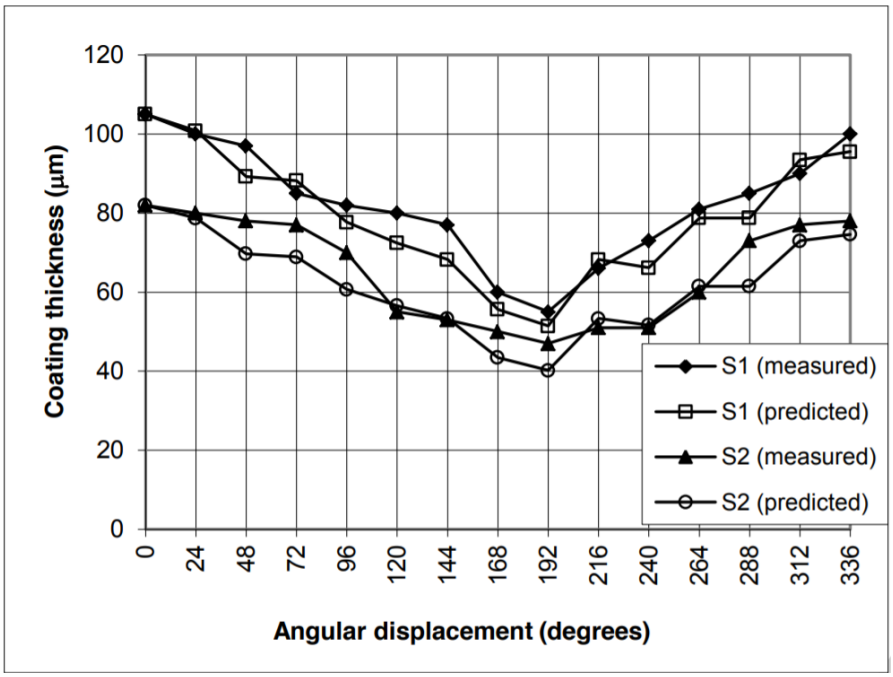

Figure 28. Comparison between measured and predicted deposition profiles for two samples. (S1 and S2) in a cluster of cylinders. (de Matos Loureiro da Silva Pereira et al., 2017)

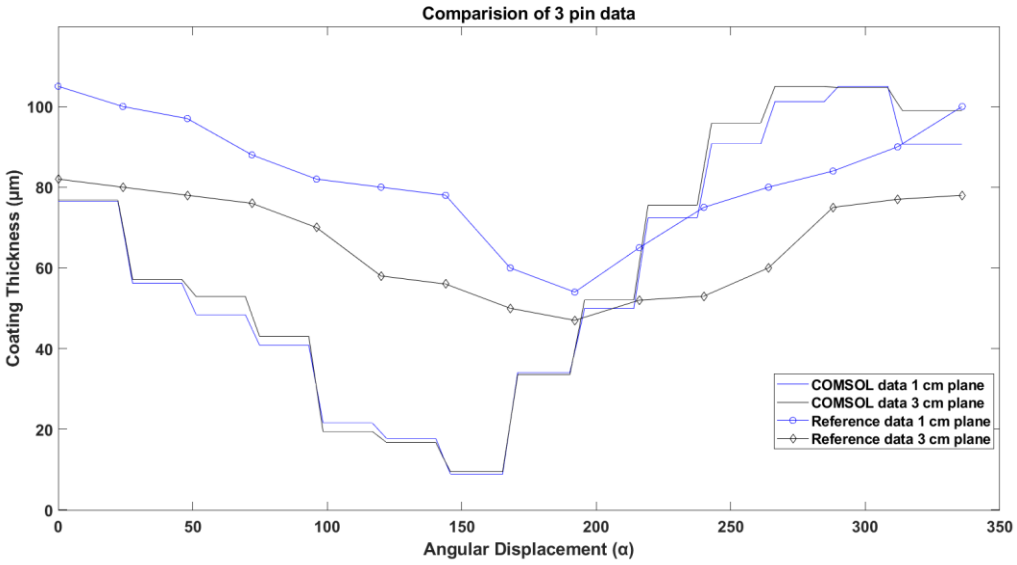

Figure 29. Comparison of thickness in two planes for the finite element model and reference data.

From the literature study, Figure 28 presents a comparison between measured and predicted deposition profiles. Besides, it illustrates the thickness distribution around the specimens as a function of angular displacement from the 0° reference point. Values 0° and 180° represent the points of highest and lowest deposition, respectively. Figure 28 further shows that the predicted coating thickness for the lowest deposition point (point affected by the shadow) is approximately 50% of the highest deposition point (de Matos Loureiro da Silva Pereira et al., 2017).

In this study, data is collected and exported to MATLAB to plot the combined curves, as shown in Figure 29. Due to limitations in the computation power, we have scaled this model to one hundredth. This plot represents the planes created in the analytical model. For comparison purposes, we have selected the planes at 0.1 and 0.3 centimeters, respectively.

The cluster's ideal arrangement is such that the blades limit the deposition on the trailing edge of other blades (act as a shadow mask) while not masking the component's leading edge. One solution could be the position of a turbine blade, for instance, identical blades at an angular displacement of 120° (for a cluster of three blades) with their trailing edges pointing to the center of the circle and their leading edges pointing away from the center of the imaginary circle. The computer model allows this arrangement to be investigated by predicting the modification in coating thickness as a function of the distance of blades from the center of rotation and rotational speed (de Matos Loureiro da Silva Pereira et al., 2017).

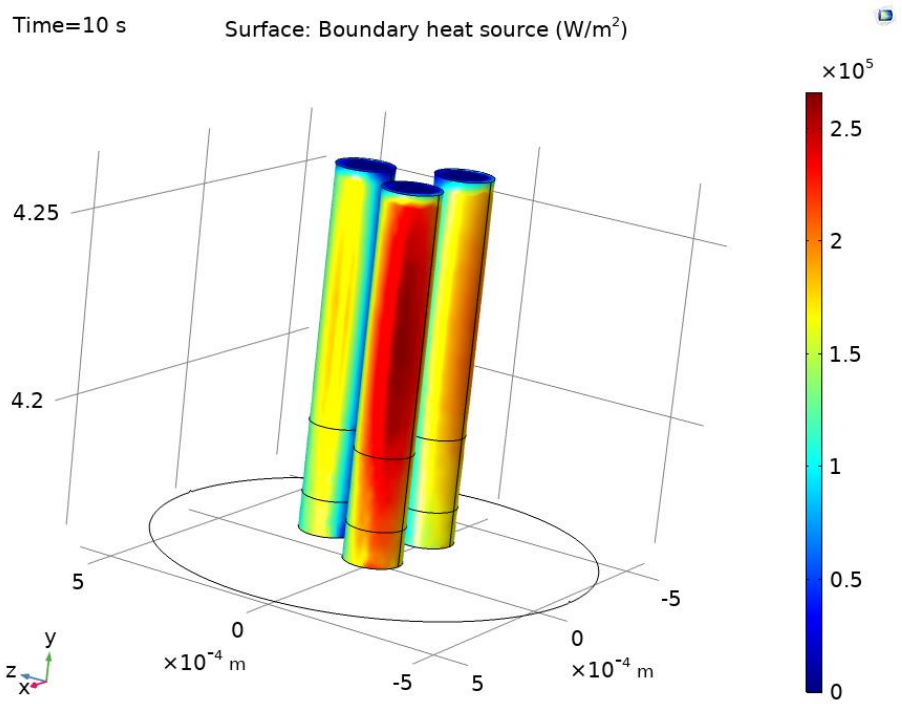

Figure 30. Finite element model result of intensity on the three-pin surface.

The finite element model defines the parameters such as medium properties, material discontinuities, ray properties, wall/surface features (to calculate deposited ray power), ray release from a grid feature (100000 rays releasing in each second interval for a minute). We can get the result in Figure 30, where the intensity has been plotted on the surface, and the planes are selected to calculate the intensity values along the arc length.

6.4 Ray Tracing Model – Turbine Blade Results

Figure 31 shows the boundary heat source intensity of the turbine blade is 200 μm compared to the values of previous results. It also depicts the thickness/Intensity values across the selected surfaces. The regions affected by the shadow effect are coated less compared to the exposed area. After simulating three different scenarios with pi/5, pi/10, 2pi/5, Figure 32 is generated. It shows the distribution along the cross-sectional plane surface.

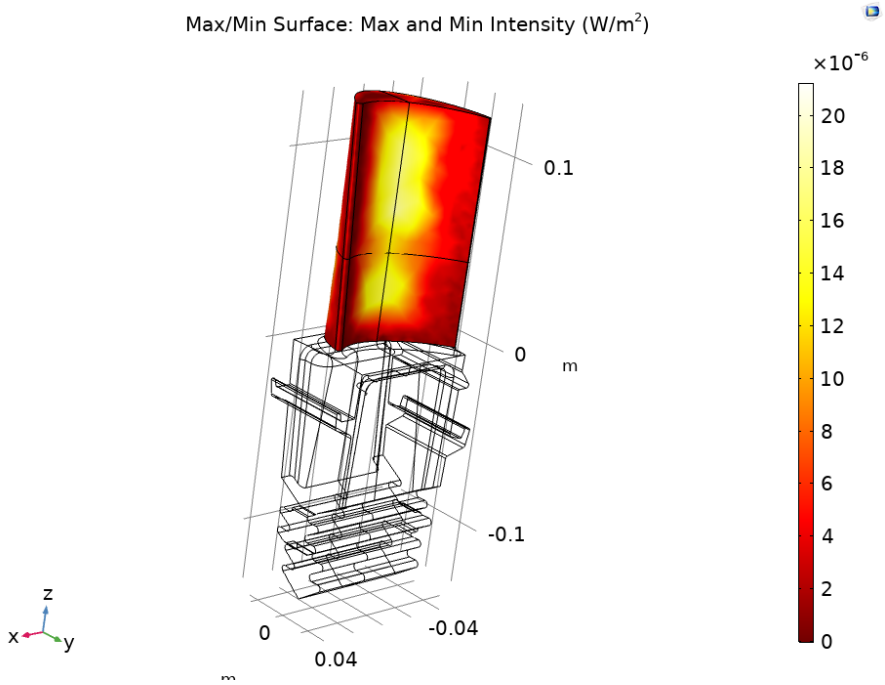

Figure 31. Turbine blade 3D surface plot

From Figure 32 at arc length of 0.016 m, which is the center part of the turbine blade coated surface, we can predict that at a speed of pi/5 rpm, the thickness is around 0.5, for a rate of 2pi/5, the thickness is 0.45, and for speed of pi/10, the thickness is 0.6. Also, in Figure 33, we can see an increase in intensity compared to time by evaluating different revolutions at a constant speed.

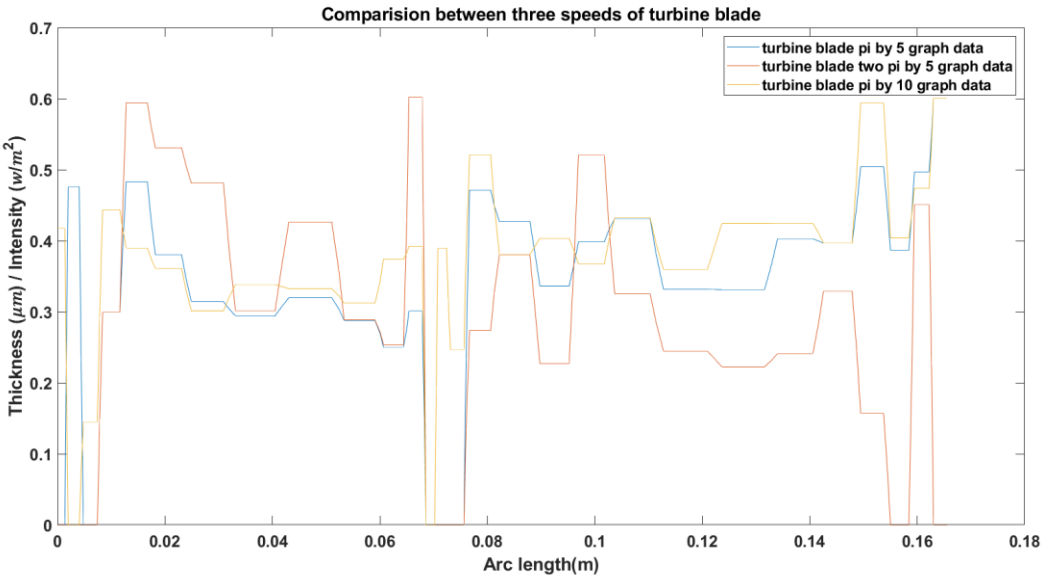

Figure 32. Comparison between three speeds of the turbine blade.

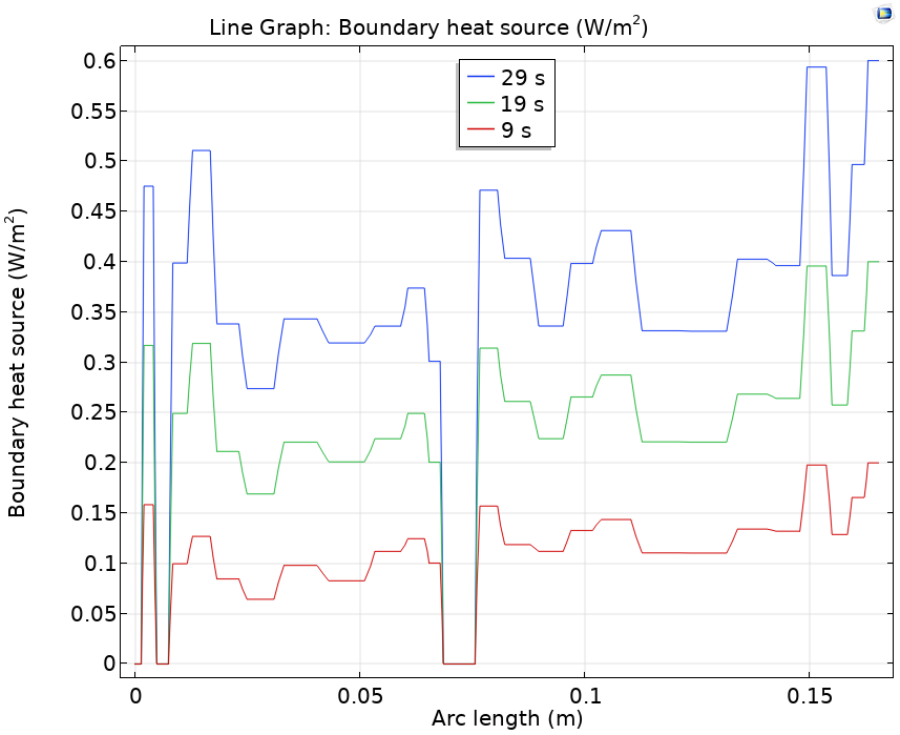

Figure 33. Comparison between different revolutions of the turbine blade at a constant speed.

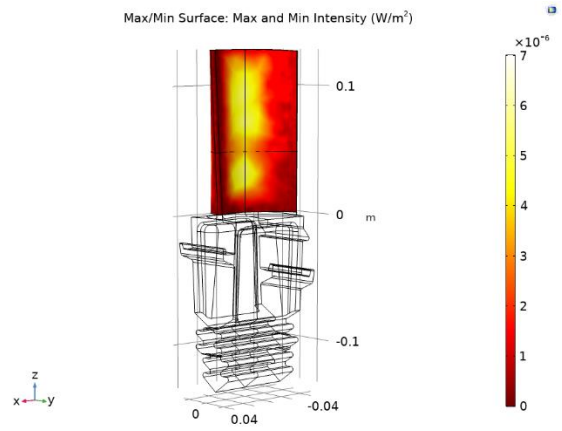

Figure 34. 3D Plot of a turbine blade at 10 seconds.

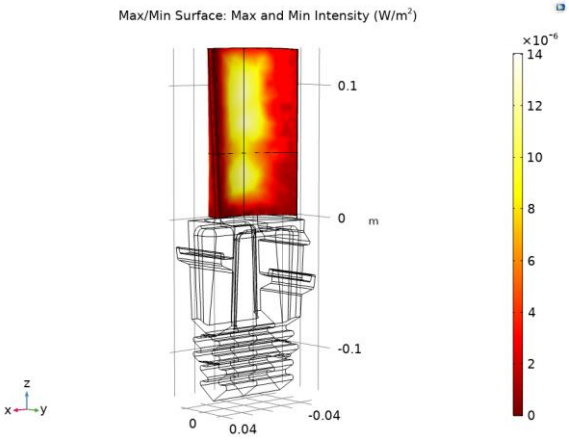

Figure 35. 3D Plot of a turbine blade at 20 seconds.

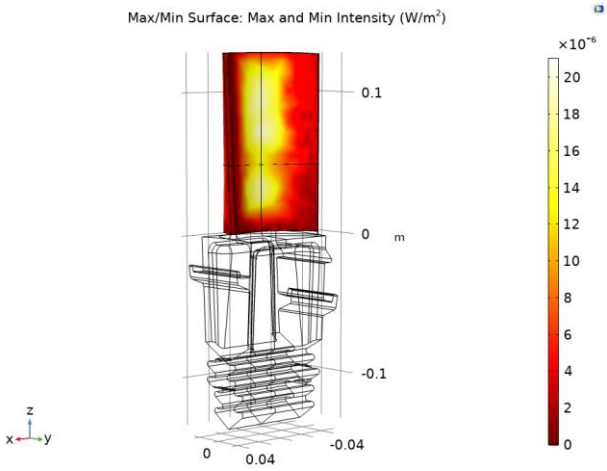

Figure 36. 3D Plot of a turbine blade at 30 seconds.

From Figure 34, Figure 35, Figure 36. we can observe that with the increase in time, the intensity of radiation is increasing.

6.5 Heat Transfer Model – Disc and Cylinder Results

The computed temperature distributions of the disc and cylinders are shown in Figure 37, respectively. As shown in the figures, the highest temperature is at the center of the surface.

To view the temperature distribution along a particular direction in Figure 37, the temperatures in the disc and cylinder's diagonal lines are plotted in Figure 38. Since both figures show the same characteristics of a cubic function, the relationship between temperature and the angle of divergence from the heating source can be fitted as a cubic polynomial function. The fitted temperature for the disc is:

$$t_{sd} = -7.4979 \times 10^{-10} \cdot \alpha^3 - 6.329 \times 10^{-4} \cdot \alpha^2 + 2.1544 \times 10^{-7} \cdot \alpha + 296.4$$

Eq. 18

Also, the fitted temperature profile for the cylinder:

$$t_{sc} = 5.6296 \times 10^{-8} \cdot \alpha^3 - 1.3465 \times 10^{-3} \cdot \alpha^2 - 1.7789 \times 10^{-5} \cdot \alpha + 295.53$$

Eq. 19

where α is the angle of divergence from the ray source.

Their maximum temperatures then normalize the temperature distributions, so the maximum normalized temperature becomes unity.

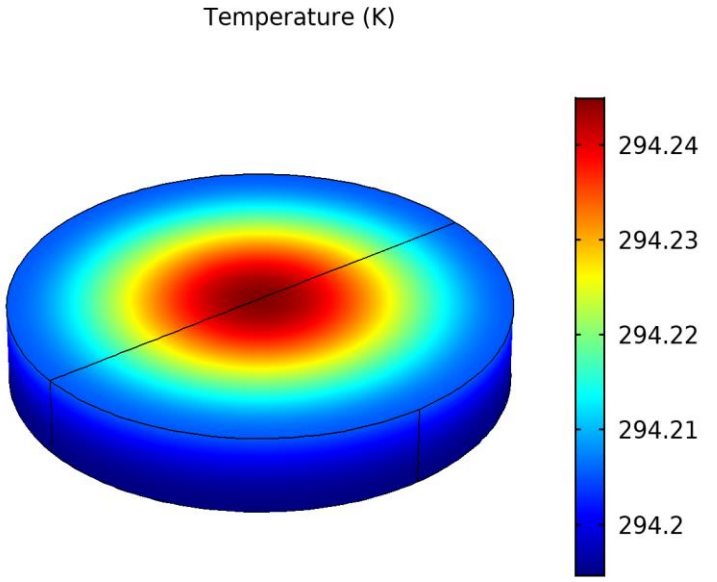

(a)

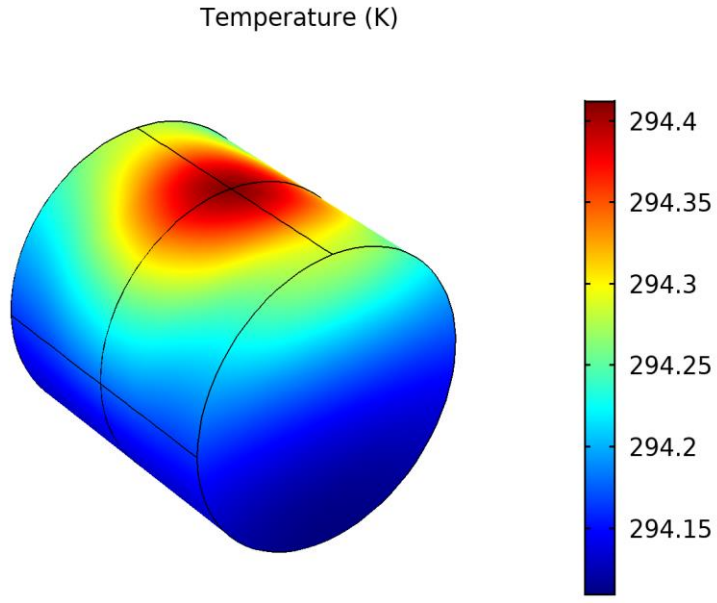

(b)

Figure 37. Temperature distribution of (a) disc and (b) cylinder.

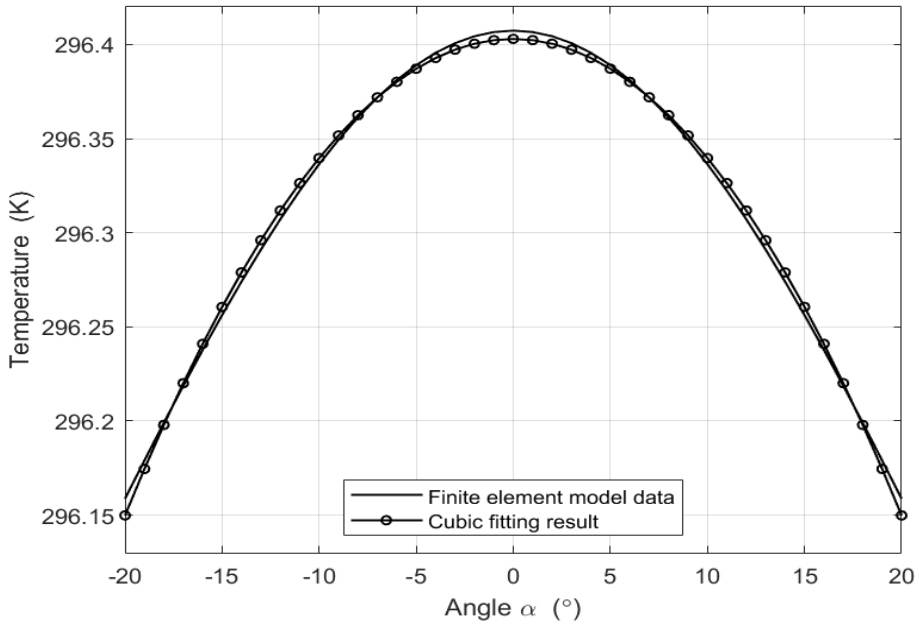

(a)

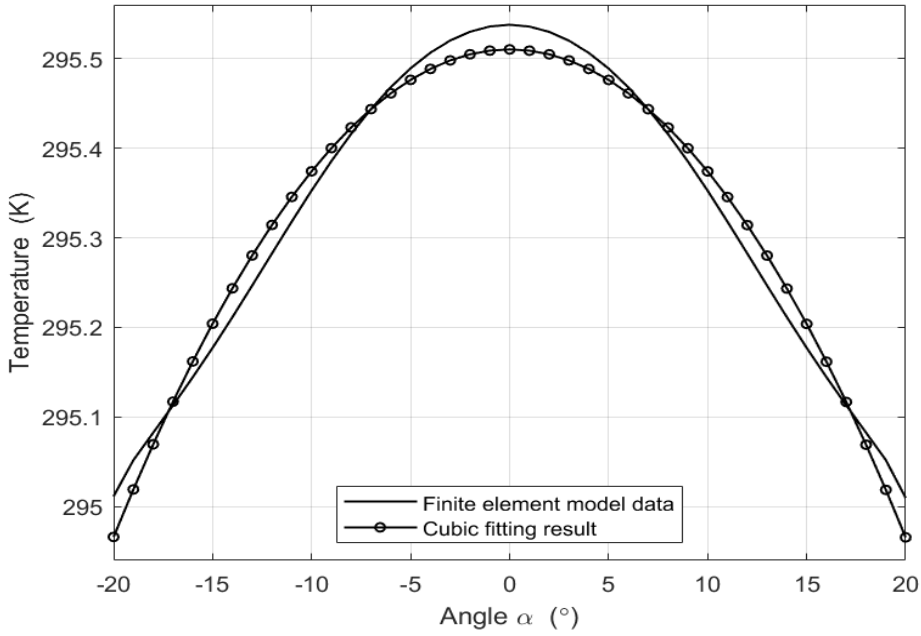

(b)

Figure 38. Predicated temperature distributions along the diagonal direction of (a) the disc and (b) the cylinder.

By fitting the cubic polynomial with the simulated model data and combining it with the analytical models solving Eq. 18, Eq. 20 for the disc, and Eq. 19, Eq. 21 for the cylinder, the relationships between the normalized coating thickness and normalized temperature t_0 can be derived, also as shown in Figure 40:

$$d_{sd}/d_{s0} = (4.6648 \times \text{ to} - 3.6662)$$

Eq. 20

$$d_{sc}/d_{s0} = (4.1033 \times \text{to} - 3.1264)$$

Eq. 21

Using Eq. 20, Eq. 21, the predicted normalized coating thicknesses of the disc and cylinder are shown in Figure 39. As shown in Figure 40, the components have the maximum coating thickness in the center, and thickness decreases gradually to the sides.

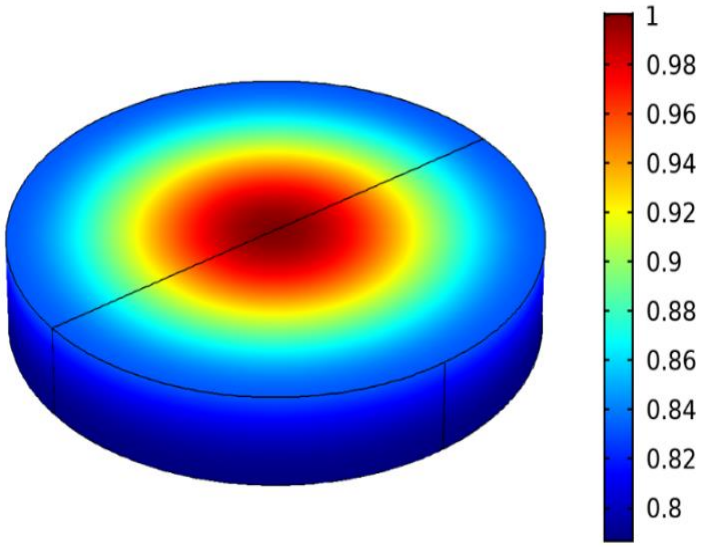

(a)

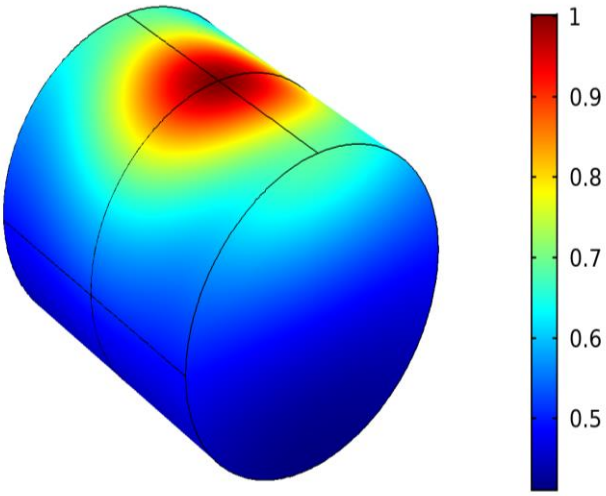

(b)

Figure 39. Predicted normalized coating thickness distributions for (a) disc, (b) cylinder.

To further check the predicted coating thickness's correctness, the comparison between the expected coating thickness and (Fuke et al., 2005) is shown in Figure 40. It shows that the predicted thickness is in excellent agreement.

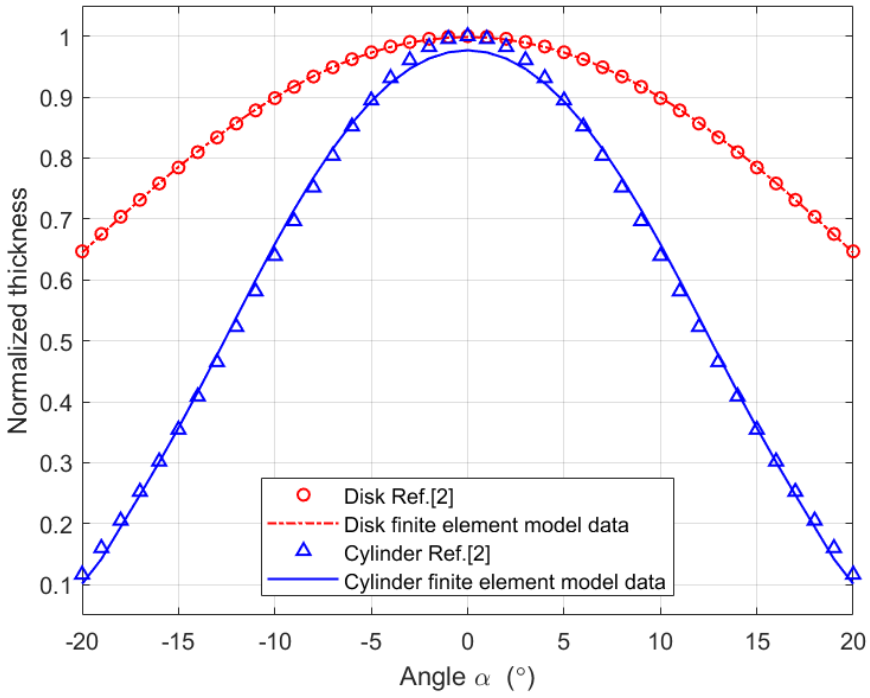

Figure 40 Predicted normalized coating thickness of disc and cylinder, compared with the (Fuke et al., 2005).

6.6 Heat Transfer Model – Three-Pin Model Results

The predicted coating thickness in the three-pin component is shown in Figure 41, assuming the maximum coating thickness is 200 μm. For each pin, the center has the maximum thickness, while the thickness decreases away towards ends.

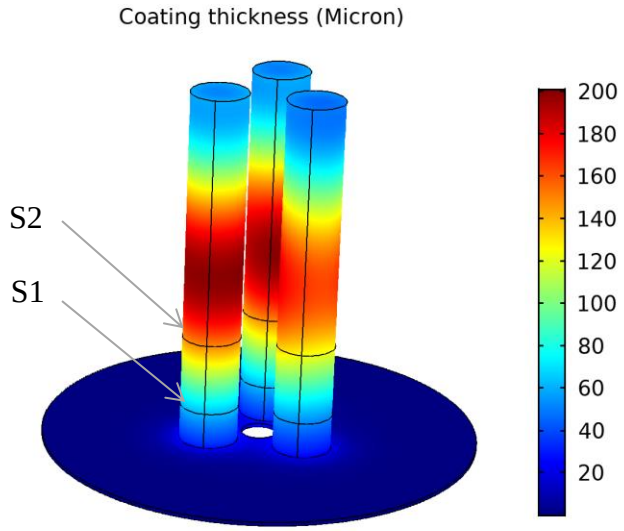

Figure 41. Predicted coating thickness in the three-pin component, assuming the maximum coating thickness is 100 μm.

To quantitatively compare with (de Matos Loureiro da Silva Pereira et al., 2017), the coating distributions in the two-section planes S1 and S2 are plotted in Figure 42. S1 and S2 are the circular profiles on the pin surface. Those are 0.03 m and 0.01 m distant from the disc surface. The predictions in this work agree reasonably well with the experimental data (de Matos Loureiro da Silva Pereira et al., 2017). The maximum coating thickness occurs at 0^0 and minimal around 150^0, which is due to the other two pins' shadow effect.

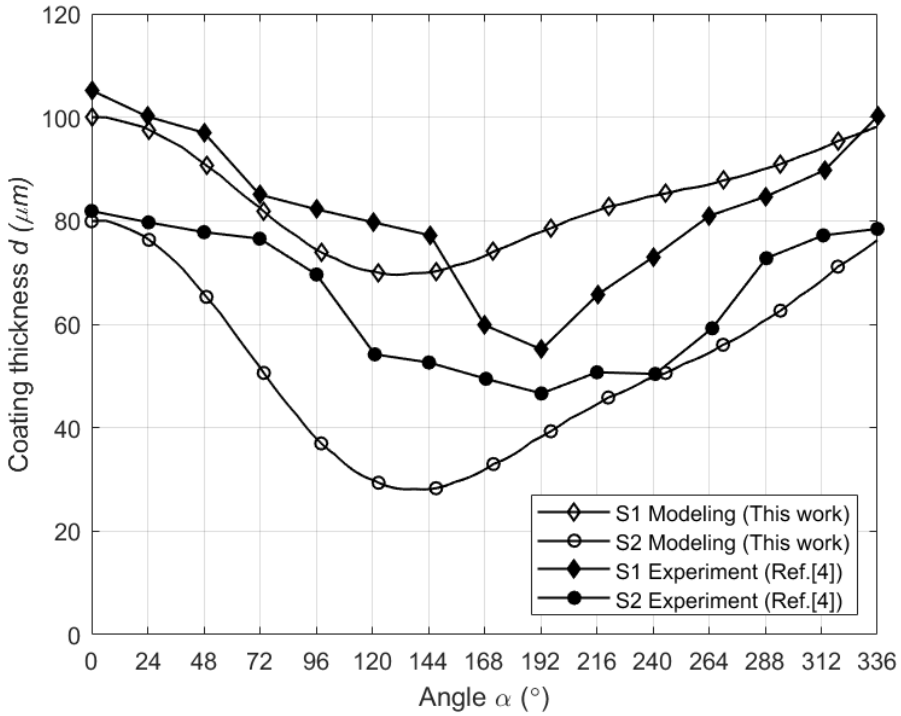

Figure 42. Predicted coating thickness distributions on two cross-sections S1 and S2 of the three-pin model, compared with the experimental points from (de Matos Loureiro da Silva Pereira et al., 2017).

6.7 Heat Transfer Model - Turbine Blade Results

The predicted coating thickness distribution in the turbine blade is shown in Figure 43, assuming the maximum coating thickness is 200 μm. The coating thickness of the blade trailing edge is higher than that of the leading edge. Thickness decreases from the trailing edge to the leading edge along the pressure side and suction side of the turbine blade.

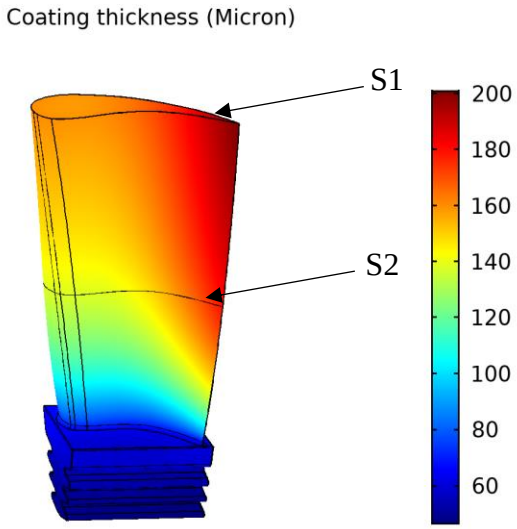

Figure 43. Predicted coating thickness distribution in the gas turbine blade model.

Figure 44 shows the predicted coating distribution along the middle plane section. It shows that trailing edge thickness is the highest. The thickness profiles of the pressure side and suction side section are almost symmetrical along the leading edge.

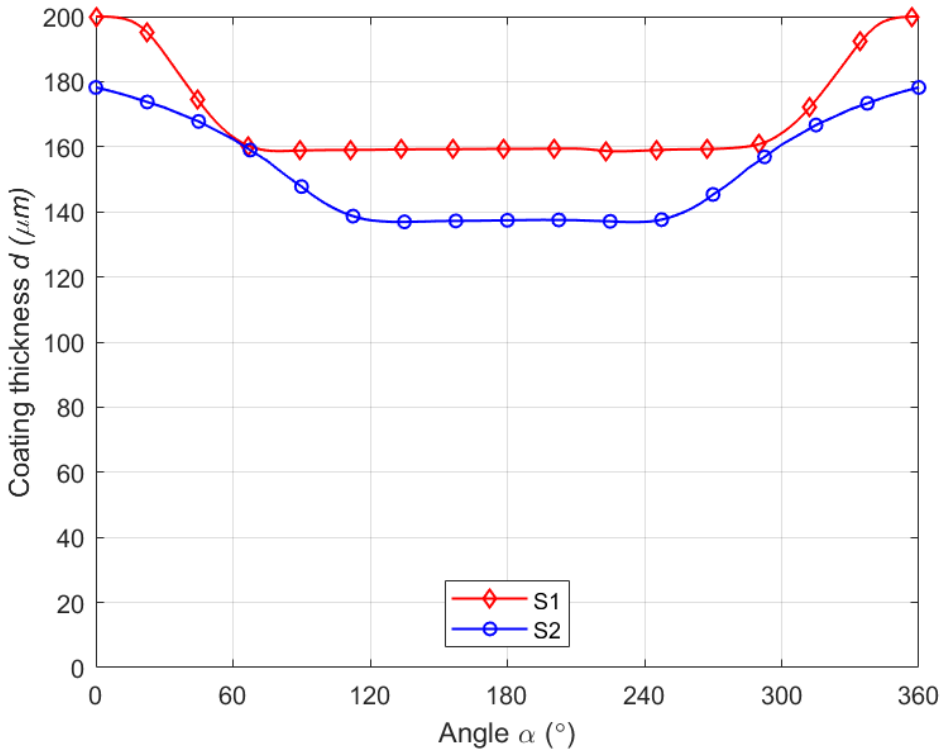

Figure 44. Predicted coating thickness along the central line of the turbine blade.

7. CONCLUSIONS

In this work, two finite element models based on the ray tracing and heat transfer methods are developed to simulate the coating thickness. The major conclusions are summarized as follows:

- The coating thickness model can be analogously compared to the computed intensity plot about the rectangular plate validation model.
- The disc and cylinder follow a similar trend by evaluating the ray-tracing method's data and comparing it with the reference. With the thickness value highest at a deposition angle of 0^o and lowest at the extremes -20^o and 20^o.
- From the ray-tracing results of the three-pin model, the minimum coating thickness at 150^o and the maximum is at 80^o and 100^o which is similar to the reference, and hence it is validated.
- All the compared models are validated using the heat transfer method by providing a new cubic polynomial based approach.
- The model is applied to the turbine blade model. For the ray-tracing model, the thickness reduces at regions affected by the shadow effect, and that the thickness at the trailing edge is more and for the heat transfer model. It shows that trailing edge thickness is the highest. The thickness profiles of the pressure side and suction side section are almost symmetrical along the leading edge.
- For the rotary turbine blade model, the simulated intensity of radiation increases with respect to time. It can predict the real scenario of coating thickness.

8. FUTURE WORK

By validating the data from various literature works, the thickness distribution on an object can be predicted using the ray tracing and heat transfer model. With extra computational efficiency, we can get more homogenous ray-tracing results by increasing the number of rays in a control volume to get optimum results. Also, more in-depth analysis of the coated regions so that the unevenly coated places can be optimized to obtain cost-effectiveness and increase efficiency.

APPENDIX A. COATING THICKNESS DATA OF A PLATE IN REFERENCE

Table A 1 Coating thickness for a thin plate, n=9

0.2	0.28	0.38	0.49	0.6	0.67	0.7	0.67	0.6	0.49	0.38	0.28	0.2
0.23	0.33	0.46	0.6	0.72	0.81	0.85	0.81	0.72	0.6	0.46	0.33	0.23
0.25	0.37	0.51	0.67	0.81	0.92	0.96	0.92	0.81	0.67	0.51	0.37	0.25
0.26	0.38	0.53	0.7	0.85	0.96	1	0.96	0.85	0.7	0.53	0.38	0.26
0.25	0.37	0.51	0.67	0.81	0.92	0.96	0.92	0.81	0.67	0.51	0.37	0.25
0.23	0.33	0.46	0.6	0.72	0.81	0.85	0.81	0.72	0.6	0.46	0.33	0.23
0.2	0.28	0.38	0.49	0.6	0.67	0.7	0.67	0.6	0.49	0.38	0.28	0.2

Table A 1 is the data generated using an analytical expression from the reference (Opsahl, 1987) with n=9, to validate it with our work. Also, Figure A1 represents the comparison between the above data and the data from the finite element package.

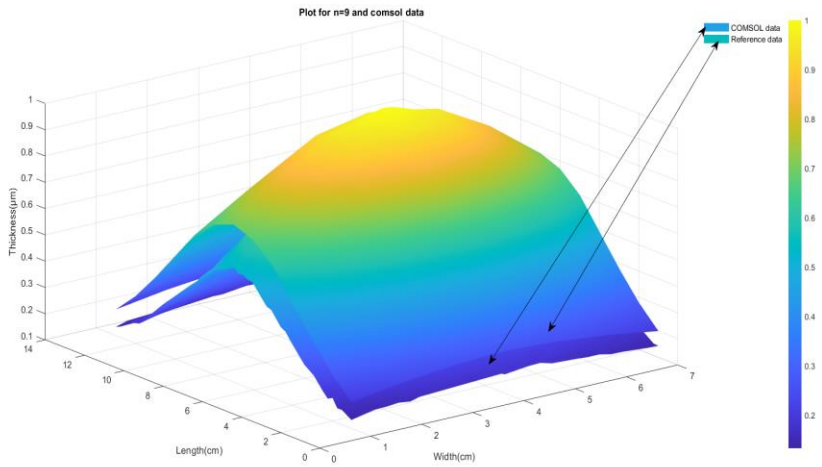

Figure A1. 3D Plot of Reference data for n=9 and finite element data.

Table A 2 Coating thickness for a thin plate, n=12

0.130093	0.203971	0.301001	0.413386	0.522963	0.604384	0.634648	0.604384	0.522963	0.413386	0.301001	0.203971	0.130093
0.159069	0.252565	0.377042	0.522963	0.666641	0.774144	0.814246	0.774144	0.666641	0.522963	0.377042	0.252565	0.159069
0.179941	0.287973	0.433037	0.604384	0.774144	0.901721	0.949421	0.901721	0.774144	0.604384	0.433037	0.287973	0.179941
0.187575	0.301001	0.453752	0.634648	0.814246	0.949421	1	0.949421	0.814246	0.634648	0.453752	0.301001	0.187575
0.179941	0.287973	0.433037	0.604384	0.774144	0.901721	0.949421	0.901721	0.774144	0.604384	0.433037	0.287973	0.179941
0.159069	0.252565	0.377042	0.522963	0.666641	0.774144	0.814246	0.774144	0.666641	0.522963	0.377042	0.252565	0.159069
0.130093	0.203971	0.301001	0.413386	0.522963	0.604384	0.634648	0.604384	0.522963	0.413386	0.301001	0.203971	0.130093

Table A 2 is the data gathered and calculated from (Opsahl, 1987) to validate it with our work. Also, Figure A2 represents the comparison between the above data and the data from the finite element model for n=12.

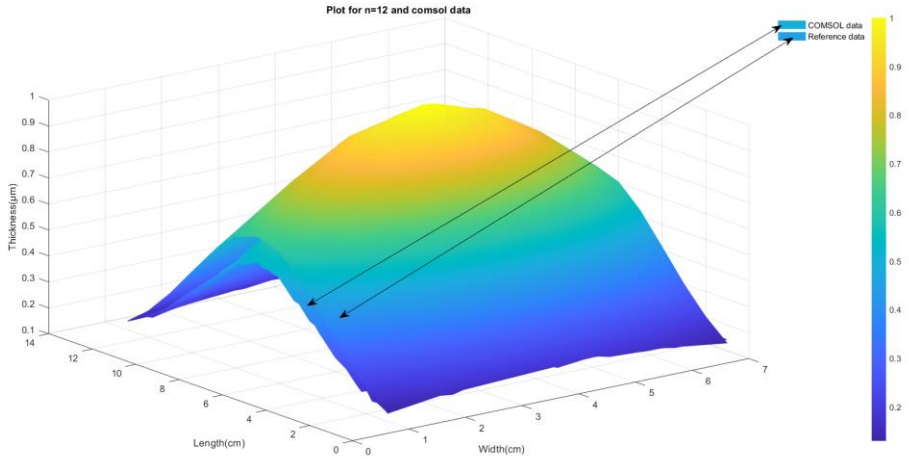

Figure A2. 3D Plot of Reference data for n=12 and finite element model data.

REFERENCES

1. Bose, S. (2018). Thermal Barrier Coatings (TBCs). In S. Bose (Ed.), High Temperature Coatings (pp. 199-299). Butterworth-Heinemann. https://doi.org/10.1016/b978-0-12-804622-7.00007-3

2. Chen, G. (2011). Non-destructive evaluation (NDE) of the failure of thermal barrier coatings. In H. Xu & H. Guo (Eds.), Thermal Barrier Coatings (pp. 243-262). Woodhead Publishing. https://doi.org/10.1533/9780857090829.3.243

3. Clarke, D. R., & Phillpot, S. R. (2005). Thermal barrier coating materials. Materials Today, 8(6), 22-29. https://doi.org/10.1016/s1369-7021(05)70934-2

4. COMSOL. (2018). The Ray Optics Module User's Guide. COMSOL https://doc.comsol.com/5.4/doc/com.comsol.help.roptics/RayOpticsModuleUsersGuide.pdf

5. De Matos Loureiro da Silva Pereira, V. E., Nicholls, J. R., & Newton, R. (2017). Modeling the EB-PVD thermal barrier coating process: Component clusters and shadow masks. Surface and Coating technology component clusters and shadow masks. Surface and Coatings Technology, 311, 307-313. https://doi.org/10.1016/j.surfcoat.2016.12.054

6. Fuke, I., Prabhu, V., & Baek, S. (2005). Computational Model for Predicting Coating Thickness in Electron Beam Physical Vapor Deposition. Journal of Manufacturing Processes, 7(2), 140-152. https://doi.org/10.1016/s1526-6125(05)70091-8

7. Guo, S., Tanaka, Y., & Kagawa, Y. (2007). Effect of interface roughness and coating thickness on interfacial shear mechanical properties of EB-PVD yttria-partially stabilized zirconia thermal barrier coating systems. Journal of the European Ceramic Society, 27(12), 3425-3431. https://doi.org/10.1016/j.jeurceramsoc.2007.02.196

8. Harper, J. M. E. (1978). Ion Beam Deposition. In J. L. Vossen & W. Kern (Eds.), Thin Film Processes (pp. 175-206). Academic Press. https://doi.org/10.1016/b978-0-12-728250-3.50010-6

9. Landau, L. D., & Lifshitz, E. M. (1987). The Classical Theory of Fields (Vol. 2). fourth edition.

10. Lang, E., Centre, C. E. C. H. T. M. I., & Commission of the European Communities. Joint Research, C. (1983). Coatings for High Temperature Applications. Applied Science Publishers. https://books.google.com/books?id=U7ZRAAAAMAAJ

11. Maissel, L. I., & Glang, R. (1970). Handbook of Thin Film Technology. McGraw-Hill. https://books.google.com/books?id=MshEAAAAIAAJ

12. Movchan, B. A. (1996). EB-PVD technology in the gas turbine industry: Present and future. JOM, 48(11), 40-45. https://doi.org/10.1007/bf03223243

13. Ni, L. Y., Liu, C., Huang, H., & Zhou, C. G. (2011). Thermal Cycling Behavior of Thermal Barrier Coatings with HVOF NiCrAlY Bond Coat. Journal of Thermal Spray Technology, 20(5), 1133. https://doi.org/10.1007/s11666-011-9647-8

14. Opsahl, C. C. (1987). Thermal Barrier Coatings: EB-PVD coating thickness prediction Rensselaer Polytechnic Institute.

15. Rees, W. S. (1995). Handbook of Deposition Technologies for Films and Coatings: Science, Technology and Applications, 2nd Edition: Edited byRointan F. Bunshah, Noyes, Park Ridge, NJ, 1994, XXVI, 861 pp., hardcover, $ 98.00, ISBN 0-81 55-13372 [https://doi.org/10.1002/adma.19950070128]. Advanced Materials, 7(1), 96.

16. Schiller, S., Heisig, U., & Panzer, S. (1975). Electron-beam trimming of thin and thick film resistor networks. 18, 38-44.

17. Wessels, H., Bode, T., Weißenfels, C., Wriggers, P., & Zohdi, T. I. (2018). Investigation of heat source modeling for selective laser melting. Computational Mechanics, 63(5), 949-970. https://doi.org/10.1007/s00466-018-1631-4

18. Xu, H. (2011). Index. In H. Xu & H. Guo (Eds.), Thermal Barrier Coatings (pp. 329-339). Woodhead Publishing. https://doi.org/10.1533/9780857090829.index

19. Xu, H., Guo, H., & Gong, S. (2008). Thermal barrier coatings. In W. Gao & Z. Li (Eds.), Developments in High-Temperature Corrosion and Protection of Materials (pp. 476-491). Woodhead Publishing. https://doi.org/10.1533/9781845694258.2.476

20. Xu, H., & Wu, J. (2011). 15 - New materials, technologies and processes in thermal barrier coatings. In H. Xu & H. Guo (Eds.), Thermal Barrier Coatings (pp. 317-328). Woodhead Publishing. https://doi.org/https://doi.org/10.1533/9780857090829.3.317

21. Yanar, N. M., Helminiak, M., Meier, G. H., & Pettit, F. S. (2010). Comparison of the Failures during Cyclic Oxidation of Yttria-Stabilized (7 to 8 Weight Percent) Zirconia Thermal Barrier Coatings Fabricated via Electron Beam Physical Vapor Deposition and Air Plasma Spray. Metallurgical and Materials Transactions A, 42(4), 905-921. https://doi.org/10.1007/s11661-010-0436-7

PUBLICATION AND PRESENTATIONS

1. Yafeng, Li., Anvesh, Dhulipalla., Jian, Zhang., Hye-Yeong., Jung, Yeon-Gill., Dan, Daehyun Koo Zhang, Jing. (2020) Finite Element Modeling of Coating Thickness Using Heat Transfer Method. CIRPJ-D-20-00410. (under review)

2. Dhulipalla, Anvesh., Uday Kumar, Budireddy., Akhil, Varupula., Jian, Zhang., Lu, Zhe., Park, Hye-Yeong., Jung, Yeon-Gill., Zhang, Jing. (2020) Synthesis and machining characteristics of novel TiC ceramic and MoS2 soft particulate reinforced aluminum alloy 7075 matrix composites. Manufacturing letters. ISSN 2213-8463, 82-86. https://doi.org/10.1016/j.mfglet.2020.04.001

3. Anvesh, Dhulipalla., Zhang, Jing. Modeling of thermal barrier coating fabrication process using electron-based physical vapor deposition (EB-PVD) on a turbine blade. (October 2018) Metal Matrix Composites and applications. Poster Presentation., Leadership Symposium, Indianapolis, Indiana.

4. Anvesh, Dhulipalla., Zhang, Jing. Modeling of thermal barrier coating fabrication process using electron-based physical vapor deposition (EB-PVD) on a turbine blade. (June 2019) Metal Injection Molding Conference, Phoenix, Arizona.

5. Anvesh Dhulipalla., Zhang Jing. Modeling of thermal barrier coating fabrication process, ASM Indianapolis. Poster Presentation. Chapter Spring Conference at Cummins, Columbus, Indiana.